A&A, 684, A139 (2024)
https://doi.org/10.1051/0004-6361/202348743

Astronomy & Astrophysics

Euclid preparation

XXXVII. Galaxy colour selections with *Euclid* and ground photometry for cluster weak-lensing analyses

Euclid Collaboration: G. F. Lesci[1,2], M. Sereno[2,3], M. Radovich[4], G. Castignani[1,2], L. Bisigello[5,4], F. Marulli[1,2,3], L. Moscardini[1,2,3], L. Baumont[6], G. Covone[7,8,9], S. Farrens[6], C. Giocoli[2,10], L. Ingoglia[1], S. Miranda La Hera[6], M. Vannier[11], A. Biviano[12,13], S. Maurogordato[11], N. Aghanim[14], A. Amara[15], S. Andreon[16], N. Auricchio[2], M. Baldi[17,2,3], S. Bardelli[2], R. Bender[18,19], C. Bodendorf[18], D. Bonino[20], E. Branchini[21,22], M. Brescia[7,8,9], J. Brinchmann[23], S. Camera[24,25,20], V. Capobianco[20], C. Carbone[26], J. Carretero[27,28], S. Casas[29], F. J. Castander[30,31], M. Castellano[32], S. Cavuoti[8,9], A. Cimatti[33], G. Congedo[34], C. J. Conselice[35], L. Conversi[36,37], Y. Copin[38], L. Corcione[20], F. Courbin[39], H. M. Courtois[40], A. Da Silva[41,42], H. Degaudenzi[43], A. M. Di Giorgio[44], J. Dinis[42,41], F. Dubath[43], C. A. J. Duncan[35,45], X. Dupac[37], S. Dusini[46], M. Farina[44], S. Ferriol[38], P. Fosalba[31,47], S. Fotopoulou[48], M. Frailis[12], E. Franceschi[2], P. Franzetti[26], M. Fumana[26], S. Galeotta[12], B. Garilli[26], B. Gillis[34], A. Grazian[4], F. Grupp[18,49], S. V. H. Haugan[50], I. Hook[51], F. Hormuth[52], A. Hornstrup[53,54], P. Hudelot[55], K. Jahnke[56], M. Kümmel[19], S. Kermiche[57], A. Kiessling[58], M. Kilbinger[59], B. Kubik[38], M. Kunz[60], H. Kurki-Suonio[61,62], S. Ligori[20], P. B. Lilje[50], V. Lindholm[61,62], I. Lloro[63], E. Maiorano[2], O. Mansutti[12], O. Marggraf[64], K. Markovic[58], N. Martinet[65], R. Massey[66], E. Medinaceli[2], M. Melchior[67], Y. Mellier[68,55], M. Meneghetti[2,3], E. Merlin[32], G. Meylan[39], M. Moresco[1,2], E. Munari[12], R. Nakajima[64], S.-M. Niemi[69], C. Padilla[27], S. Paltani[43], F. Pasian[12], K. Pedersen[70], V. Pettorino[71], S. Pires[6], G. Polenta[72], M. Poncet[73], L. A. Popa[74], L. Pozzetti[2], F. Raison[18], R. Rebolo[75,76], A. Renzi[5,46], J. Rhodes[58], G. Riccio[8], E. Romelli[12], M. Roncarelli[2], E. Rossetti[17], R. Saglia[19,18], D. Sapone[77], B. Sartoris[19,12], M. Schirmer[56], P. Schneider[64], A. Secroun[57], G. Seidel[56], S. Serrano[31,30,78], C. Sirignano[5,46], G. Sirri[3], J. Skottfelt[79], L. Stanco[46], J.-L. Starck[59], P. Tallada-Crespí[80,28], A. N. Taylor[34], H. I. Teplitz[81], I. Tereno[41,82], R. Toledo-Moreo[83], F. Torradeflot[28,80], I. Tutusaus[84], E. A. Valentijn[85], L. Valenziano[2,86], T. Vassallo[19,12], A. Veropalumbo[16,22], Y. Wang[81], J. Weller[19,18], A. Zacchei[12,13], G. Zamorani[2], J. Zoubian[57], E. Zucca[2], M. Bolzonella[2], E. Bozzo[43], C. Colodro-Conde[75], D. Di Ferdinando[3], J. Graciá-Carpio[18], S. Marcin[67], N. Mauri[33,3], C. Neissner[27,28], A. A. Nucita[87,88,89], Z. Sakr[90,84,91], V. Scottez[68,92], M. Tenti[3], M. Viel[13,12,93,94,95], M. Wiesmann[50], Y. Akrami[96,97], S. Anselmi[5,46,98], C. Baccigalupi[93,12,94,13], M. Ballardini[99,100,2], S. Borgani[101,13,12,94], A. S. Borlaff[102,103,104], S. Bruton[105], C. Burigana[106,86], R. Cabanac[84], A. Calabro[32], A. Cappi[2,11], C. S. Carvalho[82], T. Castro[12,94,13,95], G. Cañas-Herrera[69,107], K. C. Chambers[108], A. R. Cooray[109], J. Coupon[43], O. Cucciati[2], S. Davini[22], S. de la Torre[65], G. De Lucia[12], G. Desprez[110], S. Di Domizio[21,22], H. Dole[14], A. Díaz-Sánchez[111], J. A. Escartin Vigo[18], S. Escoffier[57], I. Ferrero[50], F. Finelli[2,86], L. Gabarra[5,46], K. Ganga[112], J. García-Bellido[96], F. Giacomini[3], G. Gozaliasl[113,61], S. Gwyn[114], H. Hildebrandt[115], M. Huertas-Company[75,116,117,118], A. Jimenez Muñoz[119], J. J. E. Kajava[120,121], V. Kansal[122,123], C. C. Kirkpatrick[124], L. Legrand[60], A. Loureiro[125,126], J. Macias-Perez[119], M. Magliocchetti[44], G. Mainetti[127], R. Maoli[128,32], M. Martinelli[32,129], C. J. A. P. Martins[130,23], S. Matthew[34], M. Maturi[90,131], L. Maurin[14], R. B. Metcalf[1,2], M. Migliaccio[132,133], P. Monaco[101,12,94,13], G. Morgante[2], S. Nadathur[15], L. Patrizii[3], A. Pezzotta[18], C. Porciani[64], D. Potter[134], M. Pöntinen[61], P. Reimberg[68], P.-F. Rocci[14], A. G. Sánchez[18], A. Schneider[134], M. Schultheis[11], E. Sefusatti[12,13,94], P. Simon[64], A. Spurio Mancini[135], S. A. Stanford[136], J. Steinwagner[18], G. Testera[22], R. Teyssier[137], S. Toft[54,138], S. Tosi[21,22,16], A. Troja[5,46], M. Tucci[43], J. Valiviita[61,62], and D. Vergani[2]

(Affiliations can be found after the references)

Received 27 November 2023 / Accepted 19 January 2024

ABSTRACT

Aims. We derived galaxy colour selections from *Euclid* and ground-based photometry, aiming to accurately define background galaxy samples in cluster weak-lensing analyses. These selections have been implemented in the *Euclid* data analysis pipelines for galaxy clusters.
Methods. Given any set of photometric bands, we developed a method for the calibration of optimal galaxy colour selections that maximises the selection completeness, given a threshold on purity. Such colour selections are expressed as a function of the lens redshift.
Results. We calibrated galaxy selections using simulated ground-based *griz* and *Euclid* $Y_{\rm E}J_{\rm E}H_{\rm E}$ photometry. Both selections produce a purity higher than 97%. The *griz* selection completeness ranges from 30% to 84% in the lens redshift range $z_{\rm l} \in [0.2, 0.8]$. With the full *griz*$Y_{\rm E}J_{\rm E}H_{\rm E}$ selection, the completeness improves by up to 25 percentage points, and the $z_{\rm l}$ range extends up to $z_{\rm l} = 1.5$. The calibrated colour selections are stable to changes in the sample limiting magnitudes and redshift, and the selection based on *griz* bands provides excellent results on real external datasets. Furthermore, the calibrated selections provide stable results using alternative photometric aperture definitions obtained from different ground-based telescopes. The *griz* selection is also purer at high redshift and more complete at low redshift compared to colour selections found in the literature. We find excellent agreement in terms of purity and completeness between the analysis of an independent, simulated *Euclid* galaxy catalogue and our calibration sample, except for galaxies at high redshifts, for which we obtain up to 50 percentage points higher completeness. The combination of colour and photo-z selections applied to simulated *Euclid* data yields up to 95% completeness, while the purity decreases down to 92% at high $z_{\rm l}$. We show that the calibrated colour selections provide robust results even when observations from a single band are missing from the ground-based data. Finally, we show that colour selections do not disrupt the shear calibration for stage III surveys. The first *Euclid* data releases will provide further insights into the impact of background selections on the shear calibration.

Key words. galaxies: clusters: general – galaxies: distances and redshifts – galaxies: photometry – galaxies: statistics – cosmology: observations – large-scale structure of Universe

1. Introduction

In the last decade, galaxy clusters have proven to be excellent probes for cosmological analyses (see, e.g. Mantz et al. 2015; Sereno et al. 2015; Planck Collaboration XXIV 2016; Costanzi et al. 2019; Marulli et al. 2021; Lesci et al. 2022), also allowing for the investigation of dark matter interaction models (Peter et al. 2013; Robertson et al. 2017; Eckert et al. 2022) and gas astrophysics (Vazza et al. 2017; CHEX-MATE Collaboration 2021; Zhu et al. 2021; Sereno et al. 2021). As galaxy clusters are dominated by dark matter, the functional form of their matter density profiles can be derived from N-body dark-matter-only simulations (Navarro et al. 1997; Baltz et al. 2009; Diemer & Kravtsov 2014). This allows one to estimate the mass of observed clusters, which is essential for both astrophysical and cosmological studies (Teyssier et al. 2011; Pratt et al. 2019). Currently, weak gravitational lensing is one of the most reliable methods to accurately and precisely measure cluster masses (Okabe et al. 2010; Hoekstra et al. 2012; Melchior et al. 2015; Sereno et al. 2017; Stern et al. 2019; Schrabback et al. 2021; Zohren et al. 2022). Consequently, weak-lensing cluster mass estimates are widely used in current photometric galaxy surveys, such as the Kilo Degree Survey (KiDS; Kuijken et al. 2019; Bellagamba et al. 2019), the Dark Energy Survey (DES; Abbott et al. 2020; Sevilla-Noarbe et al. 2021), and the Hyper Suprime-Cam survey (HSC; Medezinski et al. 2018; Li et al. 2022).

An accurate selection of lensed background galaxies is crucial to derive a reliable cluster weak-lensing signal. Including the contribution from foreground and cluster member galaxies may significantly dilute the weak-lensing signal (Broadhurst et al. 2005; Medezinski et al. 2007; Sifón et al. 2015; McClintock et al. 2019). For example, background selections with 90% purity dilute the cluster reduced shear measurements by 10% (see, e.g. Dietrich et al. 2019), in the absence of intrinsic alignments (Heymans & Heavens 2003). Highly pure background selections are required to properly account for this effect in weak-lensing measurements, in order to minimise the variance in the selection purity. Selection incompleteness, instead, impacts the weak-lensing noise and, in turn, the signal-to-noise ratio (S/N), which depends on the density of background sources along with the intrinsic ellipticity dispersion and measurement noise (see, e.g. Schrabback et al. 2018; Umetsu 2020). The effect of low background densities can be partially mitigated by increasing the size of the cluster-centric radial bins used in the analysis, or through the stacking of the weak-lensing signal of cluster ensembles.

Background selections based on the galaxy photometric redshift (photo-z) posteriors are commonly used in the literature (Gruen et al. 2014; Applegate et al. 2014; Melchior et al. 2017; Sereno et al. 2017; Bellagamba et al. 2019), as well as galaxy colour selections (Medezinski et al. 2010, 2018; Oguri et al. 2012; Klein et al. 2019). These selections can also be combined to significantly improve the background sample completeness and, in turn, the weak-lensing S/N. In fact, colour selections have been demonstrated to help identify galaxies with poorly defined photometric redshifts that would not have been classified as background sources through photo-z selection alone (Covone et al. 2014; Sereno et al. 2017; Bellagamba et al. 2019).

The aim of this paper is to develop a method to obtain optimal colour selections, namely with a maximal completeness given a threshold on purity, given any set of photometric filters. We provide, for the first time, colour selections expressed as a continuous function of the lens limiting redshift. This allows for a finer background definition compared to colour selections found in the literature (Medezinski et al. 2010, 2018; Oguri et al. 2012), implying a significant improvement in the weak-lensing source statistics. In view of *Euclid* and stage IV surveys, we derived colour selections on simulated data. We exploited the galaxy catalogue developed by Bisigello et al. (2020, hereafter referred to as B20), and extended by Euclid Collaboration (2023a), which includes simulated Sloan Digital Sky Survey (SDSS; Gunn et al. 1998) *griz* magnitudes and simulated *Euclid* observations in the $Y_{\rm E}J_{\rm E}H_{\rm E}$ bands. In addition, we tested the efficiency of these colour selections on real public external data and on simulations, combining them with photo-z selections.

This paper is part of a series presenting and discussing mass measurements of galaxy clusters using the *Euclid* combined clusters and weak-lensing pipeline `COMB-CL`. `COMB-CL` forms part of the global *Euclid* data processing pipeline and is responsible for measuring weak-lensing shear profiles and masses for photometrically detected clusters. A comprehensive description of the code structure and methods employed by `COMB-CL` will be presented in a forthcoming paper, but a brief overview of the pipeline can be found in the appendix of Euclid Collaboration (2023b). The galaxy colour selections presented in this paper are already implemented in `COMB-CL`.

The paper is organised as follows. In Sect. 2, we describe the dataset used for the calibration of galaxy colour selections, and in Sect. 3 we detail a general method to derive optimal colour selections. In Sect. 4, we show the selections obtained for *griz* and *griz*$Y_{\rm E}J_{\rm E}H_{\rm E}$ filter sets, validating them on external datasets. In Sect. 5 we compare the *griz* selection calibrated in this work with selections from the literature. Finally, in Sect. 6, we draw our conclusions.

2. Calibration sample

We based our analysis on the photometric catalogue developed by B20 and extended by Euclid Collaboration (2023a). This catalogue contains simulated *Euclid* $I_{\rm E}Y_{\rm E}J_{\rm E}H_{\rm E}$ aperture magnitudes[1], covering the spectral range 5500−20 000 Å, along with the Canada-France Imaging Survey (CFIS; Ibata et al. 2017) u band, for the galaxies contained in the COSMOS catalogue by Laigle et al. (2016, COSMOS15). Specifically, such photometry is based on 3″ fixed-aperture magnitudes. Despite the u band already being present in COSMOS15, B20 derived it using the same approach adopted for the other filters in order to avoid colour biases. B20 verified that this provides results that are consistent with the observed fluxes. Simulated SDSS *griz* magnitudes, spanning the wavelength range 4000−11 000 Å, are also provided in the catalogue, since observations in similar filters, such as those in *Vera C. Rubin* Observatory (*Rubin*/LSST; Ivezic et al. 2008) and DES, will be available to complement *Euclid* observations (Euclid Collaboration 2021, 2022a). Corrections for photometric offsets due to flux outside the fixed-aperture, systematic offsets, and Galactic extinction, as suggested in Laigle et al. (2016), have been applied. B20 derive simulated magnitudes through two alternative approaches. The first is a linear interpolation of the 30 medium-band and broad-band filters available in the COSMOS15 catalogue, based on the effective wavelength of the filters. The second approach is

[1] $I_{\rm E}$ band observations are supplied by the *Euclid* Visible Imager (VIS; Cropper et al. 2016), while $Y_{\rm E}J_{\rm E}H_{\rm E}$ photometry is provided by the Near-Infrared Spectrometer and Photometer (NISP; Euclid Collaboration 2022b).

based on the best theoretical template that describes the spectral energy distribution (SED) of each galaxy, assuming the COSMOS15 redshifts as the ground truth. The SED fitting is performed based on COSMOS15 bands and the template resulting in the minimum χ^2 is used to predict the expected fluxes. We refer to B20 for the details of the SED templates used, based on the model by Bruzual & Charlot (2003). The expected fluxes are then randomised 10 times considering a Gaussian distribution centred on the true flux and with standard deviation equal to the expected photometric uncertainities, scaled considering the depths listed in Table 1 of Euclid Collaboration (2023a). In this process, the $I_{\rm E}Y_{\rm E}J_{\rm E}H_{\rm E}$ magnitude errors expected for the Euclid Wide Survey are considered. Despite the fact that the *griz* photometry is based on SDSS filter transmissions, the corresponding uncertainties are based on depths that are consistent with those of DES and the Ultraviolet Near-Infrared Optical Northern Survey (UNIONS)[2]. The *ugriz* photometry provided by LSST is expected to go from 1 to 2.5 mag deeper at the end of the *Euclid* mission, depending on the photometric filter. Throughout this paper, we focus on the magnitudes derived from the best theoretical SED templates, as these estimates better reproduce absorption and emission lines that are not covered by COSMOS15 bands. We neglect u magnitudes since, due to the low u-band throughput, a 5σ depth of 25.6 mag will only be reached after 10 years of LSST observations[3]. In addition, the u band is not available in DES wide fields. We emphasise that the B20 catalogue contains all the galaxies present in the COSMOS15 sample, which is deeper than the shear samples derived from current surveys (see, e.g. Giblin et al. 2021; Gatti et al. 2021) and expected from the Euclid Wide Survey (Euclid Collaboration 2022a). As we discuss in the following, the colour selections calibrated in this study yield robust results against alternative magnitude cuts, including those that reproduce the selections adopted in current and *Euclid* cosmic shear analyses.

3. Method

In order to find a set of optimal galaxy colour-redshift relations that maximises the selection completeness given a threshold on the foreground contamination, we considered the colours given by any combination of photometric bands. This includes bands that are not adjacent in wavelength. Thus, for each colour-colour space, given a redshift lower limit, $z_{\rm l}$, corresponding to the lens redshift, we considered the following set of conditions,

$$
\begin{aligned}
&x > c_1 \vee \\
&x < c_2 \vee \\
&y > c_3 \vee \\
&y < c_4 \vee \\
&x > s_1 y + c_5 \vee \\
&x > s_2 y + c_6 \vee \\
&x < s_3 y + c_7 \vee \\
&x < s_4 y + c_8,
\end{aligned}
\tag{1}
$$

where $\vee$ is the logical "or" operator, x and y are two different colours, and c_i and s_i are colour selection parameters. Specifically, $c_1, \ldots, c_8 \in (-\infty, +\infty)$, s_1 and $s_3 \in (0, +\infty)$, while s_2 and $s_4 \in (-\infty, 0)$. The edges of the aforementioned parameter ranges are excluded, and Eq. (1) defines an irregular octagon that contains the foreground galaxies, as we show in Fig. 1. As we shall see, since we only select the colour conditions that satisfy given requirements, not all the sides of the irregular octagon may be considered. In addition, since we considered the conditions in Eq. (1) as independent, the $c_1, \ldots, c_8$ and $s_1, \ldots, s_4$ parameters are not related to each other. In particular, for each condition in Eq. (1), we derived the completeness,

$$
C_i^{nf}(z_{\rm l} \,|\, \boldsymbol{p}) := \frac{N_{{\rm sel},i}(z_{\rm g} > z_{\rm l} \,|\, \boldsymbol{p})}{N_{\rm tot}(z_{\rm g} > z_{\rm l})},
\tag{2}
$$

and the purity,

$$
\mathcal{P}_i^{nf}(z_{\rm l} \,|\, \boldsymbol{p}) := \frac{N_{{\rm sel},i}(z_{\rm g} > z_{\rm l} \,|\, \boldsymbol{p})}{N_{{\rm sel},i}(z_{\rm g} \geq 0 \,|\, \boldsymbol{p})},
\tag{3}
$$

where i is the ith colour condition index, $z_{\rm g}$ is the galaxy redshift, $\boldsymbol{p}$ is the set of colour condition parameters, $N_{{\rm sel},i}$ is the number of galaxies selected with the ith colour condition, $N_{\rm tot}$ is the total number of galaxies in the calibration sample, while the nf superscript represents quantities derived from colour conditions not fitted as a function of $z_{\rm l}$. As we shall see, we do not adopt any superscripts for the quantities derived from fitted colour conditions. In Eqs. (2) and (3), we have $i = 1 \ldots N_{\rm cond}$, where $N_{\rm cond}$ is the number of all possible colour conditions, given Eq. (1), expressed as

$$
N_{\rm cond} = 8 \, \frac{N_{\rm col}!}{(N_{\rm col} - 2)!\, 2!},
\tag{4}
$$

where $N_{\rm col}$ is the number of colours, given by

$$
N_{\rm col} = \frac{N_{\rm band}!}{(N_{\rm band} - 2)!\, 2!},
\tag{5}
$$

where $N_{\rm band}$ is the number of photometric bands.

We set requirements on completeness and purity to be satisfied by each colour condition in Eq. (1). Specifically, for a given $z_{\rm l}$, we selected the colour conditions having at least one $\boldsymbol{p}$ set

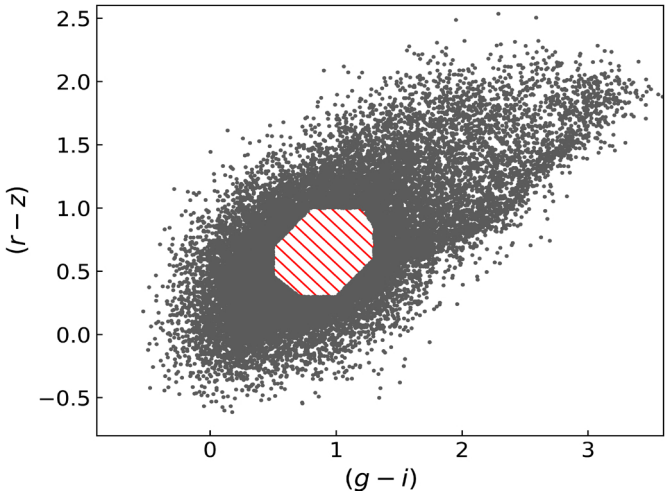

Fig. 1. Example of an uncalibrated selection in the $(r-z)-(g-i)$ colour-colour space. The grey dots represent the selected galaxy colours. Galaxies within the octagonal hatched region are excluded by applying Eq. (1). Specifically, $(r - z)$ and $(g - i)$ correspond to x and y in Eq. (1), respectively.

[2] UNIONS is carried out with the Subaru Telescope (Iye et al. 2004), the Canada-France-Hawaii Telescope (CFHT; Gwyn 2012), and the Panoramic Survey Telescope and Rapid Response System (Pan-STARRS; Chambers et al. 2016). More information at https://www.skysurvey.cc/news/

[3] https://www.lsst.org/scientists/keynumbers

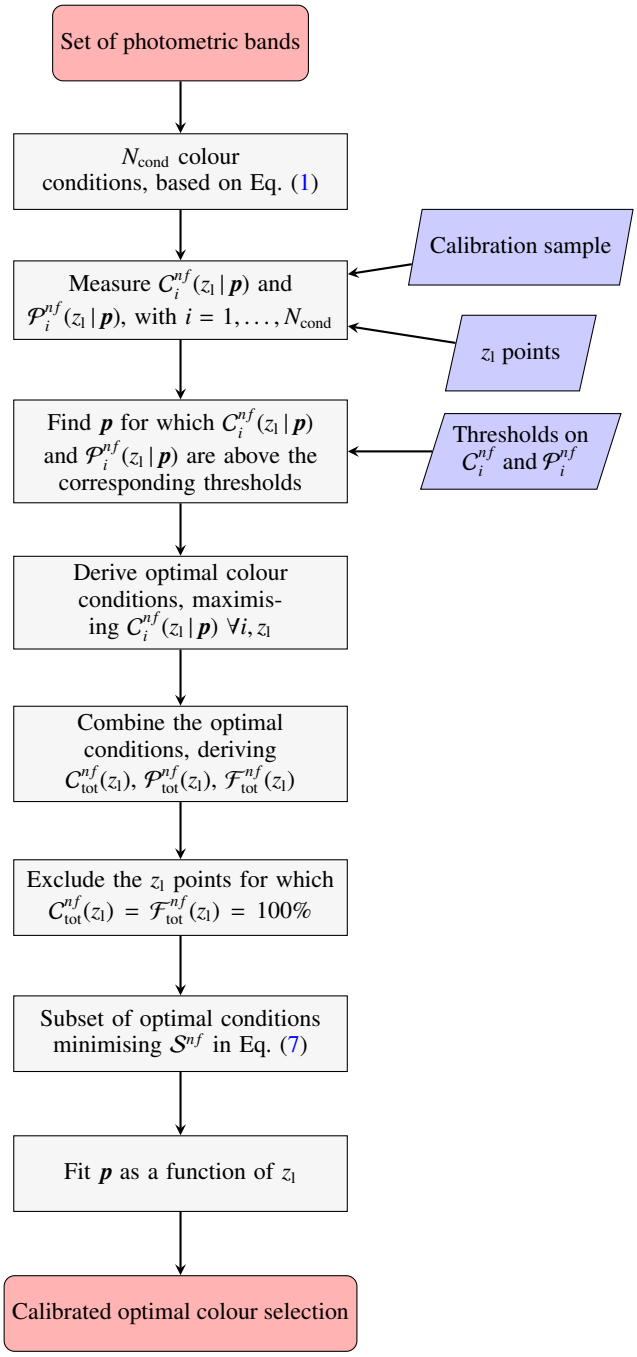

Fig. 2. Flowchart summarising the calibration process described in Sect. 3. Round red rectangles represent the start and end points of the calibration process. Grey rectangles represent processing steps, while blue trapezoids correspond to the inputs.

providing $C_i^{nf}(z_{\rm l}\,|\,\boldsymbol{p})$ and $\mathcal{P}_i^{nf}(z_{\rm l}\,|\,\boldsymbol{p})$ larger than their corresponding thresholds. We remark that $\boldsymbol{p}$ does not explicitly depend on $z_{\rm l}$ at this stage, and that $z_{\rm l}$ values are arbitrarily sampled. Setting a threshold on $C_i^{nf}(z_{\rm l}\,|\,\boldsymbol{p})$ is important for excluding colour conditions that do not significantly contribute to the total completeness, and that may appear as optimal only due to statistical fluctuations. Thus, the threshold on $C_i^{nf}(z_{\rm l}\,|\,\boldsymbol{p})$ is meant to be low compared to that on $\mathcal{P}_i^{nf}(z_{\rm l}\,|\,\boldsymbol{p})$. Indeed, as we shall detail in Sect. 4.6, impurities in the background selection imply systematic uncertainties in galaxy cluster reduced shear measurements. Highly pure selections are required to properly account for this effect, in order to minimise the scatter in purity. We discuss the choice of the thresholds on $C_i^{nf}(z_{\rm l}\,|\,\boldsymbol{p})$ and $\mathcal{P}_i^{nf}(z_{\rm l}\,|\,\boldsymbol{p})$ in greater detail in Sect. 4.1. For each colour condition in Eq. (1), with parameter values for which the conditions on $C_i^{nf}(z_{\rm l}\,|\,\boldsymbol{p})$ and $\mathcal{P}_i^{nf}(z_{\rm l}\,|\,\boldsymbol{p})$ are satisfied, we selected the $\boldsymbol{p}$ set providing the highest completeness at a given $z_{\rm l}$. In this way, we derived the set of optimal colour conditions maximising the selection completeness, given the chosen threshold on purity.

We note that the maximum $z_{\rm l}$ of the calibrated colour selections depends on the $C_i^{nf}(z_{\rm l}\,|\,\boldsymbol{p})$ and $\mathcal{P}_i^{nf}(z_{\rm l}\,|\,\boldsymbol{p})$ limits, while the minimum $z_{\rm l}$ is derived by excluding the $z_{\rm l}$ points for which $C_{\rm tot}^{nf}(z_{\rm l}) = \mathcal{F}_{\rm tot}^{nf}(z_{\rm l}) = 100\%$. Here, $C_{\rm tot}^{nf}$ and $\mathcal{F}_{\rm tot}^{nf}$ are the completeness and the foreground failure rate given by the full set of optimal colour conditions, respectively. For simplicity, we drop the dependence on $\boldsymbol{p}$ in the text. The foreground failure rate is defined as follows:

$$\mathcal{F}_{\rm tot}^{nf}(z_{\rm l}) := \frac{N_{\rm sel}(z_{\rm g} < z_{\rm l})}{N_{\rm tot}(z_{\rm g} < z_{\rm l})} = \frac{N_{\rm sel}(z_{\rm g} > z_{\rm l})}{N_{\rm tot}(z_{\rm g} < z_{\rm l})}\,\frac{1 - \mathcal{P}_{\rm tot}^{nf}(z_{\rm l})}{\mathcal{P}_{\rm tot}^{nf}(z_{\rm l})}, \tag{6}$$

where $N_{\rm sel}$ is the number of galaxies selected with all the optimal colour conditions, given a condition on $z_{\rm g}$, and $\mathcal{P}_{\rm tot}^{nf}(z_{\rm l})$ is the purity given by the full set of optimal conditions. On the right-hand side of Eq. (6), derived from Eqs. (2) and (3), we can see that $\mathcal{F}_{\rm tot}^{nf}(z_{\rm l})$ diminishes with increasing $z_{\rm l}$ if high lower limits on purity are chosen. We stress that $\mathcal{F}_{\rm tot}^{nf}(z_{\rm l}) \leq 1$ by definition.

In the selection process described above, some colour conditions may be redundant. Thus, we iteratively searched for an optimal subset of colour conditions to find the minimum number of conditions sufficient to approximately reproduce the required completeness. Specifically, at each step of this iterative process, we computed the following quantity:

$$\mathcal{S}^{nf} = \sum_{j=1}^{N} C_{\rm tot}^{nf}(z_{{\rm l},j}) - C^{nf}(z_{{\rm l},j}), \tag{7}$$

where N is the number of $z_{\rm l}$ points, $C_{\rm tot}^{nf}(z_{{\rm l},j})$ is the completeness given by all optimal conditions, while $C^{nf}(z_{{\rm l},j})$ is the completeness given by a subset of optimal conditions, computed at the jth $z_{\rm l}$ value. As the first step of this iterative process, we found the optimal colour condition minimising $\mathcal{S}^{nf}$. Then, at each iteration, we added the colour condition that, combined with the conditions selected in the previous steps, minimises $\mathcal{S}^{nf}$. We repeated this process until $\mathcal{S}^{nf}$ was lower than a given tolerance. We remark that the logical operator between colour conditions is $\vee$.

Lastly, we applied a nonlinear least squares analysis to find the best fit to the $\boldsymbol{p}$ parameters as a function of $z_{\rm l}$ for the subset of optimal colour conditions. We chose the fitting formulae which best reproduce the $z_{\rm l}$ dependence, namely polynomials, while aiming at minimising the number of free parameters in the fit.

In Fig. 2 we show a flowchart summarising the calibration process described in this section. In Fig. 3 we show an example of the iterative process detailed above, while Fig. 4 displays an example of parameter dependence on $z_{\rm l}$. Hereafter, we refer to the completeness, purity, and foreground failure rate, derived from sets of fitted colour conditions, as $C(z_{\rm l})$, $\mathcal{P}(z_{\rm l})$, and $\mathcal{F}(z_{\rm l})$, respectively. For better clarity, in Table 1 we summarise the symbols referring to the completeness functions introduced in this section.

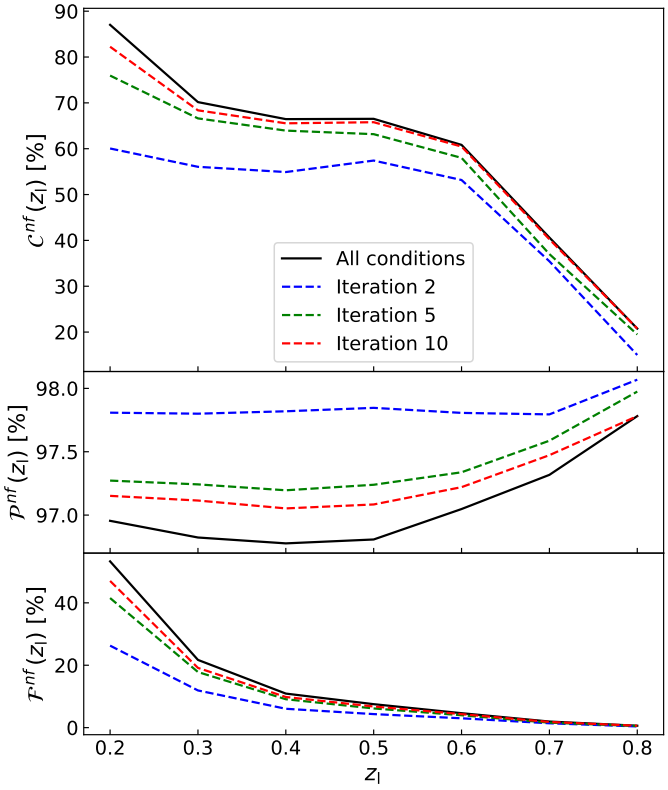

Fig. 3. Selection completeness (top panel), purity (middle panel), and foreground failure rate (bottom panel), derived from subsets of optimal colour conditions not fitted as a function of z_l, for the case of *griz* photometry. The solid black lines represent the selection given by the full set of optimal colour conditions, while the dashed lines show the selection at different steps of the iterative process detailed in Sect. 3, given by subsets of optimal conditions.

Table 1. Description of the completeness functions introduced in Sect. 3.

Symbol	Description
C_i^{nf}	Completeness of the ith colour condition, given a set of sampled parameters.
$C_{\rm tot}^{nf}$	Completeness derived through the combination of all the optimal colour conditions.
C^{nf}	Completeness given by the combination of a subset of optimal colour conditions.
C	Completeness obtained from a subset of optimal colour conditions fitted as a function of z_l.

Notes. Analogous descriptions hold for purity and foreground failure rate. The nf superscript represents quantities derived from colour conditions not fitted as a function of z_l. Optimal colour conditions satisfy the thresholds on purity and completeness, and provide maximal completeness.

4. Results

4.1. Calibration of colour selections

By applying the methods detailed in Sect. 3 and adopting the B20 calibration sample described in Sect. 2, we calibrated galaxy colour selections using ground-based and *Euclid* photometry, namely SDSS *griz* and *Euclid* $Y_{\rm E}J_{\rm E}H_{\rm E}$ filters, respectively. These selections are implemented in `COMB-CL`, and will be available for weak-lensing analyses of galaxy clusters. We

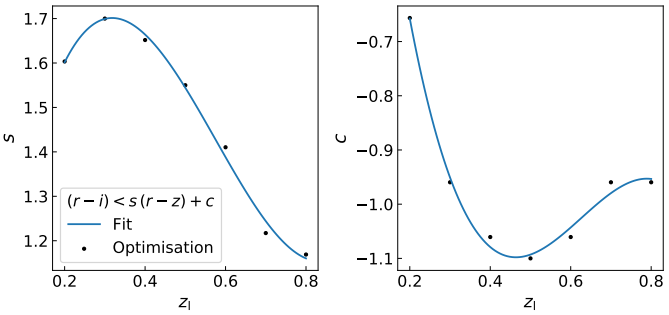

Fig. 4. Values of s (left panel) and c (right panel) parameters, from Eq. (1), as a function of z_l for the colour condition quoted in the left panel legend. The black dots represent the optimal values of s and c, while the blue curves represent the polynomial fits.

considered the following cases: ground-only, *Euclid*-only, and the combination of ground-based and *Euclid* photometry. For the cases including *Euclid* photometry, we adopted an S/N threshold for *Euclid* near-infrared observations of $(S/N)_{\rm E} > 3$, which corresponds to $Y_{\rm E} < 24.85$, $J_{\rm E} < 25.05$, and $H_{\rm E} < 24.95$ (Euclid Collaboration 2022a). In addition, we considered z_l points in the range $z_l \in [0.1, 2.5]$, assuming a precision of $\delta z_l = 0.1$ for the sampling. To derive the full set of optimal colour conditions, we imposed $C_i^{nf}(z_l\,|\,\boldsymbol{p}) > 10\%$ for the ith colour condition. For the ground-only and *Euclid*-only cases, we imposed that the purity of each colour condition is $\mathcal{P}_i^{nf}(z_l\,|\,\boldsymbol{p}) > 99\%$. We adopted a more restrictive threshold on purity for the combination of ground-based and *Euclid* photometry, corresponding to $\mathcal{P}_i^{nf}(z_l\,|\,\boldsymbol{p}) > 99.7\%$. This threshold is chosen as the larger number of colour combinations leads to a higher summation of impurities. We obtained $\mathcal{P}^{nf}(z_l) > 97\%$ for any z_l, when combining all the optimal colour conditions, as shown in Fig. 5. As we shall discuss in Sect. 4.3, the purity derived from different real datasets is stable, showing sub-percent changes, on average.

The $\mathcal{F}^{nf}(z_l)$ decrease with increasing z_l, shown in Fig. 5, is expected, as discussed in Sect. 3. In addition, for any combination of photometric bands, we found $C_{\rm tot}^{nf}(z_l) = \mathcal{F}_{\rm tot}^{nf}(z_l) = 100\%$ for $z_l = 0.1$. Consequently, we set $z_l = 0.2$ as the minimum lens redshift for the calibrated colour selections. As shown in Fig. 5, from *griz* photometry we derived a selection within $z_l \in [0.2, 0.8]$, with 84% completeness at $z_l = 0.2$, decreasing to 29% at $z_l = 0.8$. In the *Euclid*-only case, namely $Y_{\rm E}J_{\rm E}H_{\rm E}$ and $I_{\rm E}$ bands, results are not competitive with those derived from *griz* photometry. On the other hand, by combining ground-based and *Euclid* photometry, the completeness significantly increases in the z_l range covered by the *griz* selection, by up to 25 percentage points. Also the z_l range of the selection is significantly extended compared to the *griz* case, corresponding to $z_l \in [0.2, 1.5]$. Specifically, in this case we exclude the *Euclid* $I_{\rm E}$ band, as it covers a large wavelength interval, namely ~5000−10 000 Å, corresponding to the wavelength range already covered by *griz* photometry. Furthermore, the use of very broad photometric bands is not the most optimal choice for calibrating galaxy colour selections, which share similarities with photo-z estimates.

We excluded any possible redundant colour condition, as detailed in Sect. 3. In Table A.1 we show the subset of optimal colour conditions for the ground-only case, namely *griz* photometry, along with the corresponding parameter fits. The first condition quoted in Table A.1 corresponds to the one derived in the first step of the iterative process described in Sect. 3. This is analogous for the subsequent conditions. We remark that the quoted

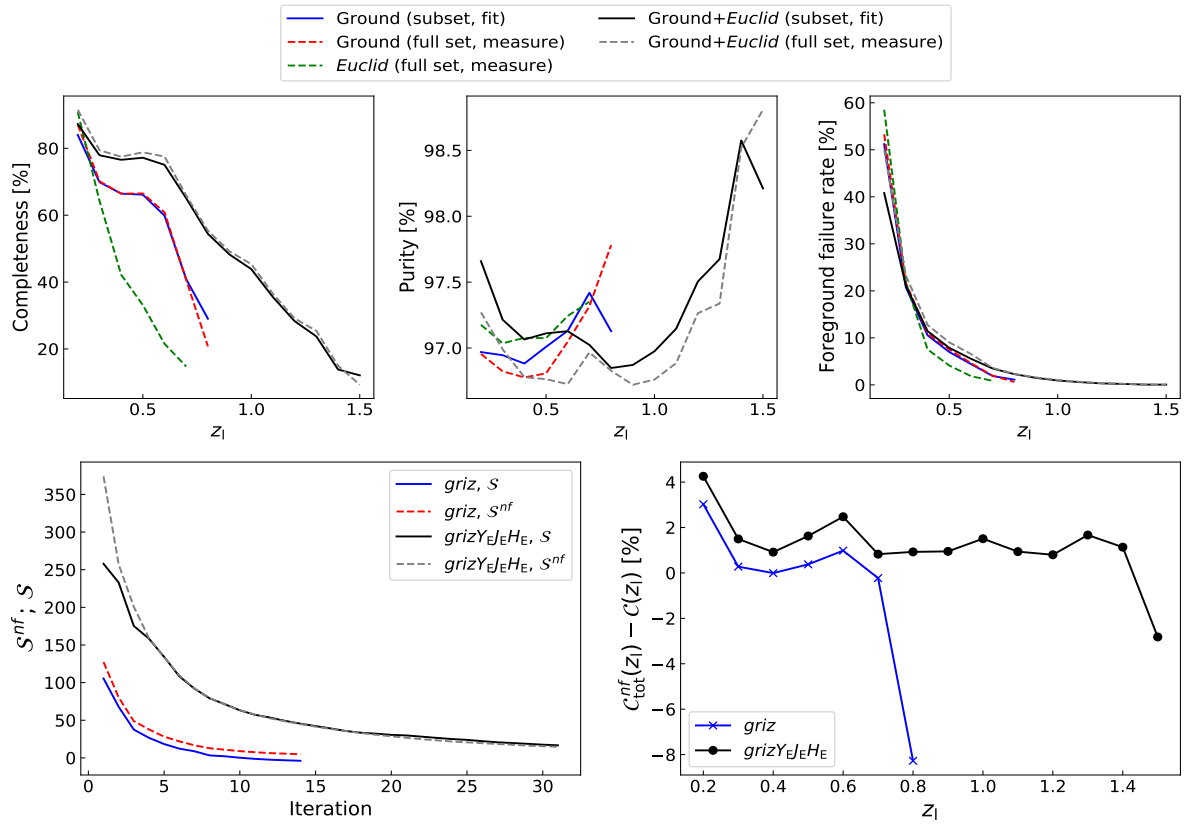

Fig. 5. Summary of the results on the colour selection optimisation, based on the B20 galaxy sample. Top panels: selection completeness (left panel), purity (central panel), and foreground failure rate (right panel), as a function of z_l. The dashed lines represent the selections derived from the full sets of optimal conditions not fitted as a function of z_l, in the case of ground-only (red), *Euclid*-only (green), and the combination of ground-based and *Euclid* bands (grey). The solid lines represent the selections obtained from the subsets of optimal conditions, with parameters fitted as a function of z_l, in the case of ground-only (blue) and for the combination of ground-based and *Euclid* bands (black). Bottom panels: in the left panel, $\mathcal{S}$ and $\mathcal{S}^{nf}$ are shown as a function of the iteration number. For the ground-based selection, using *griz* filters, $\mathcal{S}$ and $\mathcal{S}^{nf}$ are represented by solid blue and dashed red lines, respectively. For the selection derived from the combination of ground-based and *Euclid* filters, namely $grizY_EJ_EH_E$, $\mathcal{S}$ and $\mathcal{S}^{nf}$ are represented by solid black and dashed grey lines, respectively. In the right panel, the difference between C_{tot}^{nf} and C is shown, for the *griz* (blue lines) and $grizY_EJ_EH_E$ (black lines) selections.

conditions have different ranges of validity in z_l. Analogous information is listed in Table A.2 for the combination of ground-based and *Euclid* photometry, corresponding to $grizY_EJ_EH_E$ filters. We neglected the optimisation and parameter fitting for the *Euclid*-only case, as we have already shown that it does not provide competitive completeness values.

In Fig. 5 we show the results for the selections obtained from the subsets of optimal conditions, with parameters fitted as a function of z_l. For both *griz* and $grizY_EJ_EH_E$ photometry, such fitted selections well reproduce those given by the full sets of optimal conditions. To quantify the goodness of the colour condition parameter fits, we defined a parameter analogous to $\mathcal{S}^{nf}$ in Eq. (7), namely $\mathcal{S}$. This parameter quantifies the difference between C_{tot}^{nf}, that is the completeness given by the full set of optimal conditions not fitted as a function of z_l, and C, which is the completeness given by the subset of optimal colour conditions fitted as a function of z_l. As shown in Fig. 5, $\mathcal{S}$ does not perfectly match $\mathcal{S}^{nf}$, for both *griz* and $grizY_EJ_EH_E$ selections. This is due to the fact that the $c_1, \ldots, c_8$, $s_1, \ldots, s_4$ parameters in Eq. (1) do not always show a simple dependence on z_l. Despite the fact that better parameter fits could be achieved by adopting an arbitrarily high order polynomial as the model, we set a 4th order polynomial as the highest-degree functional form for describing these parameters (see Tables A.1 and A.2). As shown in Fig. 5, C is underestimated by at most 4 percentage points. We verified that adding further conditions to these selections, that is, lowering the $\mathcal{S}$ threshold down to 0, provides sub-percent level improvements in the selection completeness, on average. We remark that, in order to derive colour selections not defined in z_l bins, the final selection completeness is slightly degraded compared to C_{tot}^{nf} for some z_l values. In realistic cluster weak-lensing analyses, however, we expect this to statistically increase the galaxy background completeness. When colour selections are defined on finite sets of z_l points, the background galaxies are excluded based on the z_l precision adopted in the colour selection calibration.

4.2. Dependence on magnitude and redshift selections

To verify the robustness of the *griz* selection with respect to alternative magnitude cuts, we applied the selection $i < 24.4$, corresponding to the peak value of the i magnitude distribution in the B20 catalogue. We also investigate the selection for the subsample with $i < 23.4$, which is a threshold similar to the DES i band limit (Sevilla-Noarbe et al. 2021). In both cases, we derived higher $\mathcal{P}(z_l)$ and lower $\mathcal{F}(z_l)$, compared to what we found from the calibration sample used in Sect. 4.1, namely the one with $(S/N)_E > 3$ and $i \leq i_{max}$, where $i_{max} = 24.9$ is the maximum i magnitude in the sample (see Fig. 6). In the case with $i < 24.4$, $C(z_l)$ is close to that from the calibration sample,

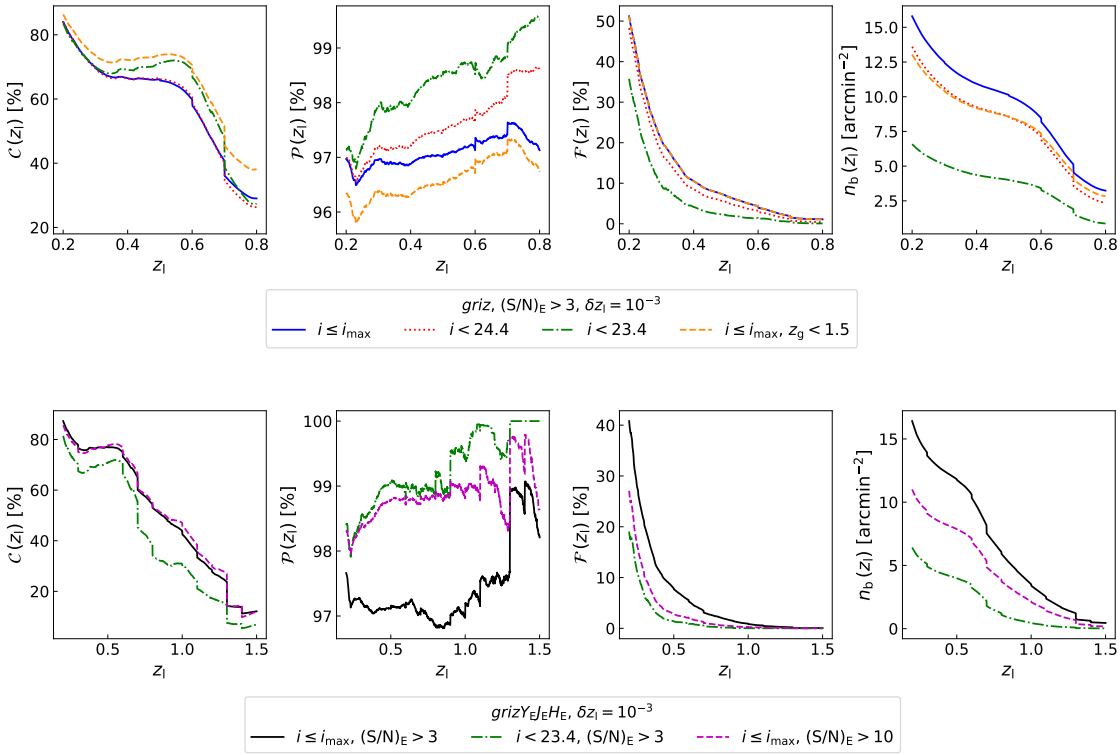

Fig. 6. Results from the fitted colour selections derived in Sect. 4.1, assuming the alternative magnitude and redshift selections described in Sect. 4.2. From left to right: completeness, purity, foreground failure rate, and background density as a function of z_l. The assumed z_l precision is $\delta z_l = 10^{-3}$. Top panels: efficiency of the *griz* selection, detailed in Table A.1, applied to the B20 catalogue with $(S/N)_E > 3$ and $i \leq i_{max}$ (blue solid lines), to its subsample including galaxies with $i < 24.4$ (red dotted lines), to the case with $i < 23.4$ (green dash-dotted lines), and to the sample with $z_g < 1.5$ (orange dashed lines). Bottom panels: efficiency of the $grizY_EJ_EH_E$ selection, detailed in Table A.2, applied to the B20 catalogue with $(S/N)_E > 3$ and $i \leq i_{max}$ (black solid lines), to its subsample with $i < 23.4$ (green dash-dotted lines), and to the subsample with $(S/N)_E > 10$ (magenta dashed lines).

while for $i < 23.4$ we derived higher completeness, on average. In addition, as the bulk of the redshift distribution in the calibration sample, described in Sect. 2, extends up to $z_g \sim 4$, we applied the *griz* selection to the galaxy sample with redshift $z_g < 1.5$, $(S/N)_E > 3$, and $i \leq i_{max}$. In Fig. 6, we can see that this redshift limit provides $\mathcal{F}(z_l)$ values that are identical to those derived from the calibration sample, which is expected since $\mathcal{F}(z_l)$ does not depend on the maximum redshift of the sample, while the completeness increases by up to 10 percentage points and the purity is at most 1 percentage point lower. We note that the computation of $C(z_l)$ and $\mathcal{F}(z_l)$ is made relative to the sample under consideration. In other words, they refer to galaxy populations defined by given magnitude and redshift limits. We measured the aforementioned colour selections by assuming a z_l precision of $\delta z_l = 10^{-3}$. This δz_l value is one order of magnitude lower (i.e. one order of magnitude higher precision) than the typical galaxy cluster photometric redshift uncertainty in current surveys (see, e.g. Rykoff et al. 2016; Maturi et al. 2019) and *Euclid* (Euclid Collaboration 2019). Consequently, the $\delta z_l = 10^{-3}$ precision ensures the reliability of the colour condition fits for galaxy cluster background selections. We remark that we assumed $\delta z_l = 0.1$ for the z_l sampling in the calibration process.

In Fig. 6 we show the efficiency of the $grizY_EJ_EH_E$ selection, computed by adopting $\delta z_l = 10^{-3}$, applied to the B20 calibration sample, with $(S/N)_E > 3$ and $i \leq i_{max}$. We found analogous selections from the subsample with $i < 23.4$ and from the one with $(S/N)_E > 10$. Specifically, in both cases, we derived higher $\mathcal{P}(z_l)$ and lower $\mathcal{F}(z_l)$, in agreement with what we found from the *griz* selection. In addition, the increase in the minimum *Euclid* S/N does not significantly change the completeness, while the $i < 23.4$ limit decreases $C(z_l)$ by at most 18 percentage points. As we obtained excellent $\mathcal{P}(z_l)$ and $\mathcal{F}(z_l)$ estimates from these tests, we conclude that both *griz* and $grizY_EJ_EH_E$ selections are stable and reliable with respect to changes in the sample limiting magnitude and redshift. In addition, we note that brighter galaxy samples provide lower foreground contamination. This is expected, as faint galaxies have more scattered colour-redshift relations.

In Fig. 6 we show the density of background galaxies, $n_b(z_l)$, defined as the number of selected galaxies with $z_g > z_l$ per square arcmin. For both *griz* and $grizY_EJ_EH_E$ selections, $n_b(z_l) = 16\,\mathrm{arcmin}^{-2}$ at $z_l = 0.2$ for $i \leq i_{max}$ and $(S/N)_E > 3$, decreasing with increasing z_l. In both colour selections, the $i < 23.4$ limit implies the largest decrease in $n_b(z_l)$, providing $n_b(z_l) < 7\,\mathrm{arcmin}^{-2}$. In addition, for the *griz* selection, the $i < 24.4$ and $z_g < 1.5$ limits provide consistent results on $n_b(z_l)$, showing a difference of at most $3\,\mathrm{arcmin}^{-2}$ compared to that derived from the calibration sample. With regard to the $grizY_EJ_EH_E$ selection, the $(S/N)_E > 10$ limit implies a decrease in $n_b(z_l)$ of up to $5\,\mathrm{arcmin}^{-2}$ at low z_l, while $n_b(z_l)$ becomes compatible with that derived from the calibration sample for $z_l > 1$.

4.3. *griz* selection validation on real data

To further assess the reliability of the *griz* colour selection detailed in Sect. 4.1, we applied it to external datasets obtained from real observations. In particular, we considered the VIMOS

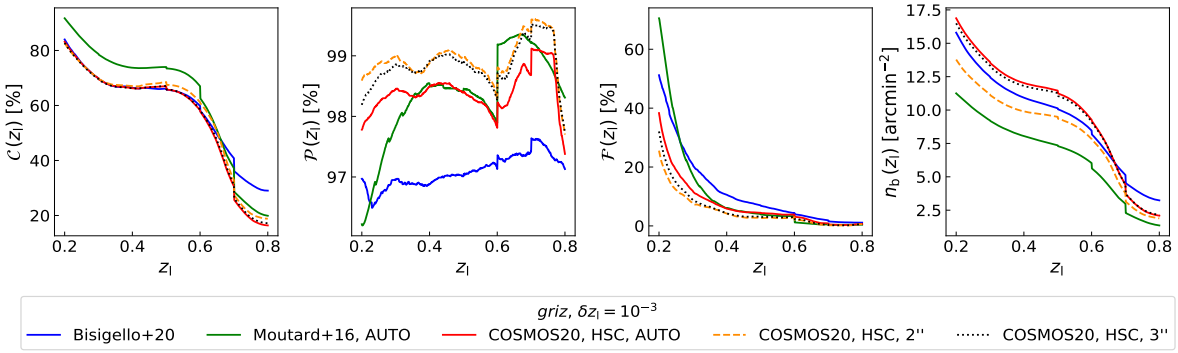

Fig. 7. Results of the application of the fitted colour selection based on *griz* photometry, reported in Table A.1, to the datasets introduced in Sect. 4.3. From left to right: completeness, purity, foreground failure rate, and background density as a function of z_l. The assumed z_l precision is $\delta z_l = 10^{-3}$. The *griz* selection is applied to the B20 catalogue with magnitude limits corresponding to those used in the calibration process (blue solid lines), to the full depth Moutard et al. (2016) catalogue (green solid lines), and to the Weaver et al. (2022) catalogue with HSC Kron, 2″ and 3″ aperture magnitudes (solid red, dashed orange and dotted black lines, respectively), for which we imposed $i < 25$.

Public Extragalactic Redshift Survey (VIPERS; Guzzo et al. 2014) Multi-Lambda Survey (VMLS) photometric catalogue by Moutard et al. (2016), including Canada-France-Hawaii Telescope Legacy Survey (CFHTLS; Hudelot et al. 2012) *griz* Kron aperture magnitudes (Kron 1980). This catalogue covers 22 deg^2 and provides reliable photometric redshifts for more than one million galaxies with a typical accuracy of $\sigma_z \leq 0.04$, and a fraction of catastrophic failures lower than 2% down to $i \sim 23$. These statistics are based on VIPERS data, complemented with the most secure redshifts selected from other spectroscopic surveys. We remind that in VIPERS a colour-colour pre-selection was employed to enhance the effective sampling of the VIMOS spectrograph. Nevertheless, the VIPERS selection does not introduce any significant colour bias above $z \sim 0.6$ (Guzzo et al. 2014). In addition, as we shall see in the following, the selection completeness and purity obtained from the VMLS dataset do not exhibit remarkable deviations from those obtained from other galaxy samples. In Fig. 7 we can see that, by applying the *griz* selection to the VMLS sample, we derived higher $\mathcal{P}(z_l)$ and lower $\mathcal{F}(z_l)$ compared to what we found from the B20 catalogue, on average. This agrees with what we found in Sect. 4.2, as the Moutard et al. (2016) catalogue is shallower than the B20 sample. For the same reason, $n_b(z_l)$ is 3 arcmin^{-2} lower, on average. In addition, the completeness is up to 8 percentage points higher for $z_l < 0.6$, becoming lower for higher z_l values.

We also applied the *griz* selection to the COSMOS CLASSIC catalogue by Weaver et al. (2022, COSMOS20), which reaches the same photometric redshift precision as COSMOS15, namely $\sigma_z/(1+z) = 0.007$, at almost one magnitude deeper. We considered *griz* Kron, 2″ and 3″ aperture magnitudes from HSC. In addition, we selected galaxies with a photometric redshift derived from at least 30 bands, and with $i < 25$, in order to consider a sample with highly reliable redshift estimates. By adopting more complex selection criteria, which may involve galaxies with photometric redshifts derived from a shared set of photometric bands, we do not expect remarkable differences in the results. Similar results for the cases with Kron, 2″ and 3″ aperture magnitudes are shown in Fig. 7. Compared to what we derived from the B20 sample, the completeness is similar, with the largest differences at $z_l > 0.6$. In addition, $\mathcal{F}(z_l)$ is lower and $\mathcal{P}(z_l)$ is higher for any z_l. For Kron and 3″ aperture magnitudes, $n_b(z_l)$ is slightly higher compared to that obtained from the B20 sample, on average. Lower $n_b(z_l)$ values show up for the 2″ aperture magnitudes, which is expected as we applied the same magnitude limit for each photometric aperture definition. Indeed, for these tests we did not include aperture correction terms. Lastly, comparing the purity derived from the COSMOS20 and VMLS samples, we note that for $z_l > 0.3$ the differences are below 1 percentage point, on average. Thus, we conclude that the *griz* selection provides robust and reliable results on real data.

4.4. Validation on Flagship v2.1

We tested the colour selections calibrated in Sect. 4.1 on the *Euclid* Flagship galaxy catalogue v2.1.10 (Euclid Collaboration, in prep.), which is currently the best simulated *Euclid* galaxy catalogue available. This catalogue is based on an N-body simulation with around 4 trillion particles with mass $m_p \sim 10^9\, h^{-1}\, M_\odot$. A flat Λ cold dark matter (ΛCDM) cosmological model was assumed, with matter density parameter $\Omega_m = 0.319$, baryon density parameter $\Omega_b = 0.049$, dark energy density parameter $\Omega_\Lambda = 0.681$, scalar spectral index $n_s = 0.96$, Hubble parameter $h = H_0/(100\,\mathrm{km\,s^{-1}\,Mpc^{-1}}) = 0.67$, and standard deviation of linear density fluctuations on $8\,h^{-1}$ Mpc scales $\sigma_8 = 0.83$. The haloes were identified using `Rockstar` (Behroozi et al. 2013), and then populated with a halo occupation distribution model which was calibrated to reproduce observables such as clustering statistics as a function of galaxy luminosity. The galaxy SED templates used are the COSMOS templates from Ilbert et al. (2009), based on the models by Bruzual & Charlot (2003) and Polletta et al. (2007). In addition, galaxy photo-z probability distribution functions, namely $p(z_g)$, are included in Flagship, derived through a Nearest Neighbours Photometric Redshifts (NNPZ) pipeline (Euclid Collaboration 2020).

From the Flagship catalogue, we extracted a lightcone within RA $\in [158°, 160°]$ and Dec $\in [12°, 15°]$, considering the galaxies in the whole redshift range covered by the simulation, namely $z_g \in [0, 3]$. Specifically, z_g is the galaxy true redshift, and we verified that the contribution of peculiar velocities does not significantly change the results. We focused on 2″ aperture LSST *ugrizy* and *Euclid* $I_E Y_E J_E H_E$ photometry, as the simulated fluxes estimated for other ground-based surveys do not account for observational noise. Specifically, the photometric noise takes into account the depth expected in the southern hemisphere at the time of the third data release (DR3) for the Euclid Wide Survey. The LSST and *Euclid* 10σ magnitude limits, which are proxies for extended sources, correspond to $u < 24.4$, $g < 25.6$, $r < 25.7$, $i < 25.0$, $z < 24.3$, $y < 23.1$, $I_E < 25$, $Y_E < 23.5$, $J_E < 23.5$,

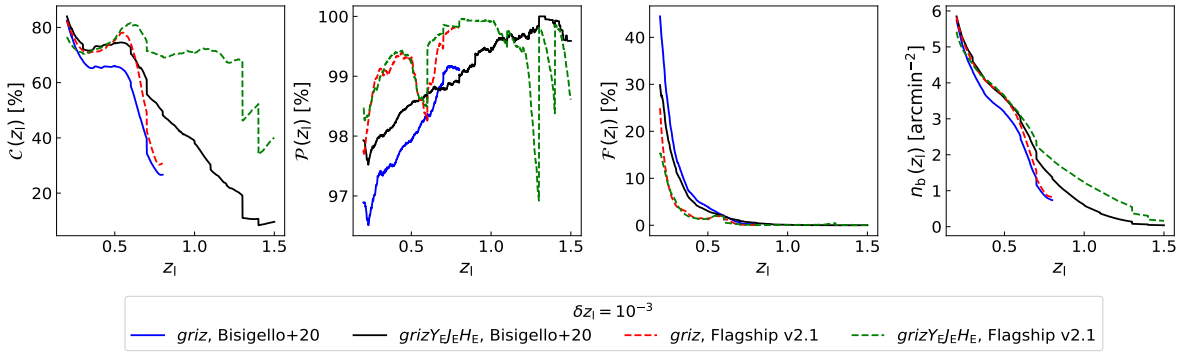

Fig. 8. Application of the calibrated colour selections to the Flagship simulated sample described in Sect. 4.4. From left to right: completeness, purity, foreground failure rate, and background density as a function of z_l, from the fitted colour selections based on *griz* and $grizY_EJ_EH_E$ bands, adopting 5σ magnitude limits. The assumed z_l precision is $\delta z_l = 10^{-3}$. The solid blue and solid black lines represent the *griz* and $grizY_EJ_EH_E$ selections, respectively, applied to the B20 catalogue. The dashed red and dashed green curves represent the *griz* and $grizY_EJ_EH_E$ selections, respectively, applied to the Flagship v2.1 catalogue (Euclid Collaboration, in prep.).

and $H_E < 23.5$. The fluxes we considered are not reddened due to Milky Way extinction, consistent with the analyses performed in the previous sections.

In Fig. 8, we show the application of *griz* and $grizY_EJ_EH_E$ selections to Flagship. For this test, we assumed 5σ magnitude cuts for LSST *ugrizy* and *Euclid* $I_EY_EJ_EH_E$ bands. In addition, we show results from the B20 sample in Fig. 8, for which we assumed 5σ magnitude cuts rescaled from the 10σ limits listed in Euclid Collaboration (2023a, Table 1). We found that $n_b(z_l)$ derived from Flagship agrees with that obtained from the B20 sample. The largest differences, of about 1 arcmin^{-2}, arise when the $grizY_EJ_EH_E$ selection is applied. We note that $n_b(z_l) \sim 0$ for $z_l \sim 1.5$, implying that lenses at these values of z_l may not exhibit significant weak-lensing signals. Nevertheless, we verified that $n_b(z_l)$ is enhanced at any z_l when the selection defined for *Euclid* weak-lensing analyses (Laureijs et al. 2011; Euclid Collaboration 2022a) is assumed. This selection consists in a 10σ cut in the I_E band, corresponding to $I_E < 25$ for a $2''$ aperture, yielding a galaxy density of around 39 arcmin^{-2} when applied to the Flagship dataset. In fact, in this case $n_b(z_l)$ ranges from 30 arcmin^{-2} at low z_l to 3 arcmin^{-2} at $z_l = 1.5$.

As shown in Fig. 8, on average we obtained higher $\mathcal{P}(z_l)$ and lower $\mathcal{F}(z_l)$ for $z_l < 1$ from Flagship, compared to what we derived from the B20 sample. For the *griz* selection case, $\mathcal{C}(z_l)$ agrees with that derived from the B20 sample, with the largest differences, of up to 16 percentage points, at $z_l \sim 0.5$. Larger differences in $\mathcal{C}(z_l)$ are obtained from the $grizY_EJ_EH_E$ selection. From Flagship we obtained $\mathcal{C}(z_l)$ up to 10 percentage points larger for $z_l < 0.6$, and up to 50 percentage points larger for higher z_l. We verified that this discrepancy in the completeness, in the case of the $grizY_EJ_EH_E$ selection, is not significantly attenuated through the assumption of 3σ and 10σ magnitude limits on both B20 and Flagship catalogues. Analogous results were obtained by assuming limits corresponding to the magnitude distribution peaks derived from the B20 catalogue, namely $g < 24.9$, $r < 24.6$, $i < 24.3$, $z < 24.1$, $Y_E < 23.8$, $J_E < 23.6$, and $H_E < 23.5$. Moreover, we verified that the $grizY_EJ_EH_E$ selection completeness does not remarkably vary by assuming the *Euclid* weak-lensing selection defined above, namely $I_E < 25$. Similar results are obtained by considering the photometric errors expected for the DR2 of the Euclid Wide Survey, assuming the corresponding 3σ, 5σ, and 10σ magnitude cuts. For each of the alternative magnitude cuts discussed in this section, we found that the $grizY_EJ_EH_E$ selection yields a purity up to 3 percentage points higher at $z_l > 1.2$ when it is applied to the B20 catalogue, compared to what is derived from Flagship. At $z_l < 1.2$, instead, the purity obtained from B20 is 1 percentage point lower, on average. Furthermore, the alternative magnitude cuts do not remarkably impact the selection purity at any z_l.

We additionally adopted SDSS fluxes, which do not include photometric noise, in place of LSST fluxes in Flagship. In this case, the completeness is up to 35 percentage points larger than that derived from the B20 sample, and the purity approaches 100% for $z_l > 1$, which is similar to what we derived from the B20 sample (see Fig. 8). Thus, the selection based on SDSS photometry is less complete and purer compared to that obtained from LSST magnitudes.

Differences in the completeness derived from the Flagship and B20 samples may originate from distinct assumptions on the physical properties of the galaxies, such as dust extinction, stellar age, nebular emission lines, or on the assumed intrinsic spectral energy distributions. This could be indicated by a different fraction of star forming galaxies in the two samples. Following B20, galaxies are classified as star forming if the following condition is satisfied,

$$\log_{10}(\mathrm{sSFR}/\mathrm{yr}^{-1}) > -10.5, \tag{8}$$

where sSFR is the specific star formation rate, derived from the best SED template in the catalogue by B20. We verified that, for $z_g > 1$, the fraction of star forming galaxies in Flagship is consistent within 1 percentage point with that derived from the catalogue by B20. Thus, we conclude that the completeness differences between the Flagship and B20 samples are not due to different star forming galaxy populations. We also verified that the $\log_{10}(\mathrm{sSFR}/\mathrm{yr}^{-1})$ distributions derived from the two datasets are compatible, having peaks at ~ -8.13 and ~ -8.35 in B20 and Flagship, respectively. The agreement of these peak values is well within 1σ of the $\log_{10}(\mathrm{sSFR}/\mathrm{yr}^{-1})$ distributions. We will be able to further investigate such completeness differences through the analysis of the first data release of the Euclid Deep Survey.

4.5. Comparison with photo-z selections

To compare the colour selections derived in this work to selections based on the galaxy $p(z_g)$, commonly referred to as photo-z selections, we analysed the Flagship sample described in Sect. 4.4. We considered only the galaxies with a $p(z_g)$ estimate obtained with the NNPZ pipeline (Euclid Collaboration 2020). The NNPZ photo-zs are designed to work well for

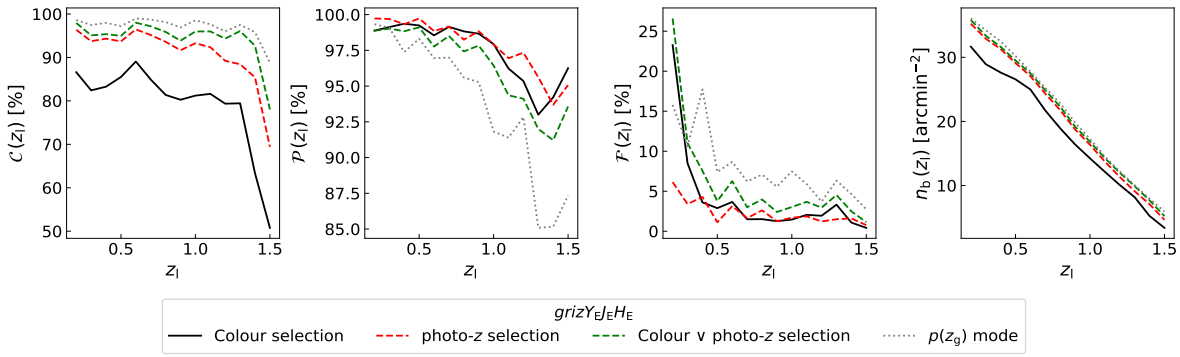

Fig. 9. Comparison of colour and photo-z selections. From left to right: completeness, purity, foreground failure rate, and background density as a function of z_l, obtained from Flagship v2.1. The solid black lines represent the $grizY_EJ_EH_E$ selection. The dashed green lines show the combination, through the ∨ logical operator, of $grizY_EJ_EH_E$ and photo-z selection (Eq. (9)). The dashed red lines represent the photo-z selection, while the dotted black lines represent the selection based on the $p(z_g)$ mode.

galaxies that are expected to be used in core *Euclid* weak-lensing science, namely with 5σ limits on the I_E band. Thus we imposed $I_E < 25.75$, along with 5σ limits on the $Y_EJ_EH_E$ bands, namely $Y_E < 24.25$, $J_E < 24.25$, $H_E < 24.25$. Specifically, we adopted the following photo-z selection,

$$z_g^{\rm min} > z_l, \tag{9}$$

where $z_g^{\rm min}$ is the minimum of the interval containing 95% of the probability around the first mode of $p(z_g)$, namely $\bar{z}_g$. We chose $z_g^{\rm min}$ in order to derive $\mathcal{P}(z_l)$ values which are compatible with those obtained from colour selections. We verified that adding a condition on the width of $p(z_g)$ in Eq. (9) does not impact the results. Specifically, for the latter test, we considered the additional condition $\mathcal{A} > \mathcal{A}_{\rm min}$, where $\mathcal{A}$ is the integrated probability around $\bar{z}_g$, computed within the redshift points, which are the closest to $\bar{z}_g$, having an associated probability of $0.2p(\bar{z}_g)$. We verified that imposing $\mathcal{A}_{\rm min} = 0$ or $\mathcal{A}_{\rm min} = 0.8$ leads to compatible purity values with sub-percent differences on average. However, $\mathcal{A}_{\rm min} = 0.8$ lowers the photo-z selection completeness by around 20 percentage points at all z_l. Consequently, we assumed $\mathcal{A}_{\rm min} = 0$.

To perform a fair comparison of colour and photo-z selections, we considered only the $grizY_EJ_EH_E$ colour selection in this section. This is because photo-zs in Flagship were derived from the combination of ground-based and *Euclid* photometry. In Fig. 9, we show that the $grizY_EJ_EH_E$ selection provides, on average, a completeness 15 percentage points lower than that of the photo-z selection, with similar contamination. By combining $grizY_EJ_EH_E$ and photo-z selections, through the logical operator ∨, the completeness increases by up to 10 percentage points with respect to the case of photo-z selection alone, amounting to $C(z_l) \sim 95\%$ for $z_l < 1.4$. These preliminary tests confirm the importance of the combination of colour and photo-z selections, as it leads to significantly more complete background galaxy samples. We also remark that increasing the selection completeness is key to reduce biases in the shear calibration parameters due to background selections, as we shall detail in Sect. 4.6. The analysis of *Euclid* data will allow for a detailed investigation of the optimal photo-z selections for galaxy cluster weak-lensing analyses, outlining the synergies with colour selections. For example, colour selections applied to *Euclid* data could provide more robust background samples for massive or nearby galaxy clusters, as derived by Medezinski et al. (2018). Leveraging colour selections also serves as a valuable cross-validation method for addressing the effect of unknown systematic uncertainties in photo-z estimates. Lastly, Fig. 9 shows the selection based only on the first mode of $p(z_g)$. Specifically, in this case we selected the galaxies with $\bar{z}_g > z_l$. Despite $C(z_l) > 90\%$ at all z_l, the purity is up to 10 percentage points lower than that obtained from the $grizY_EJ_EH_E$ selection.

4.6. Impact on shear measurements

In cluster weak-lensing analyses, the inclusion of foreground sources in the shear measurements may significantly dilute the signal (Broadhurst et al. 2005; Medezinski et al. 2007; Sifón et al. 2015; McClintock et al. 2019). As discussed in the previous sections, the calibrated colour selections provide $\mathcal{P}(z_l) < 1$. To assess the impact of impurities on shear measurements, we can express the cluster reduced tangential shear unaffected by contamination as follows (Dietrich et al. 2019):

$$g_{\rm t,true}(z_l) = \frac{g_{\rm t}(z_l)}{\mathcal{P}(z_l)}, \tag{10}$$

where $g_{\rm t}(z_l)$ is the measured cluster reduced tangential shear at redshift z_l. As the calibrated colour selections yield $\mathcal{P}(z_l) > 0.97$, we expect at most a 3% bias on the reduced tangential shear. In addition, as discussed in Sect. 4.3, $\mathcal{P}(z_l)$ derived from different observed datasets with only ground-based photometry shows a scatter below 1 percentage point. This scatter in $\mathcal{P}(z_l)$ is lower than the systematic uncertainty on galaxy shape measurements for stage III surveys, as we shall discuss in the following. We remark that $\mathcal{P}(z_l)$ is derived from reference fields, while galaxy clusters are overdense compared to the cosmic mean. Thus, contamination from cluster galaxies must be properly accounted for in Eq. (10) (see, e.g. Gruen et al. 2014; Dietrich et al. 2019). Nevertheless, such contamination is consistent with zero in the typical cluster-centric radial range adopted for mass calibration, namely at radii larger than $300\,h^{-1}$ kpc (see, e.g. Medezinski et al. 2018; Bellagamba et al. 2019).

Furthermore, galaxy shear calibration is usually statistically derived, based on observed and simulated galaxy samples. Nevertheless, through galaxy cluster background selections, some galaxy populations may be systematically excluded. This may invalidate the statistical estimate of the shape multiplicative bias, namely m, depending on the shear measurement technique and on the actual properties of the data (Heymans et al. 2012; Miller et al. 2013; Hildebrandt et al. 2016).

The typical uncertainty on m found for stage III surveys ranges in the interval $\delta m \in [1 \times 10^{-2}, 3 \times 10^{-2}]$ (see,

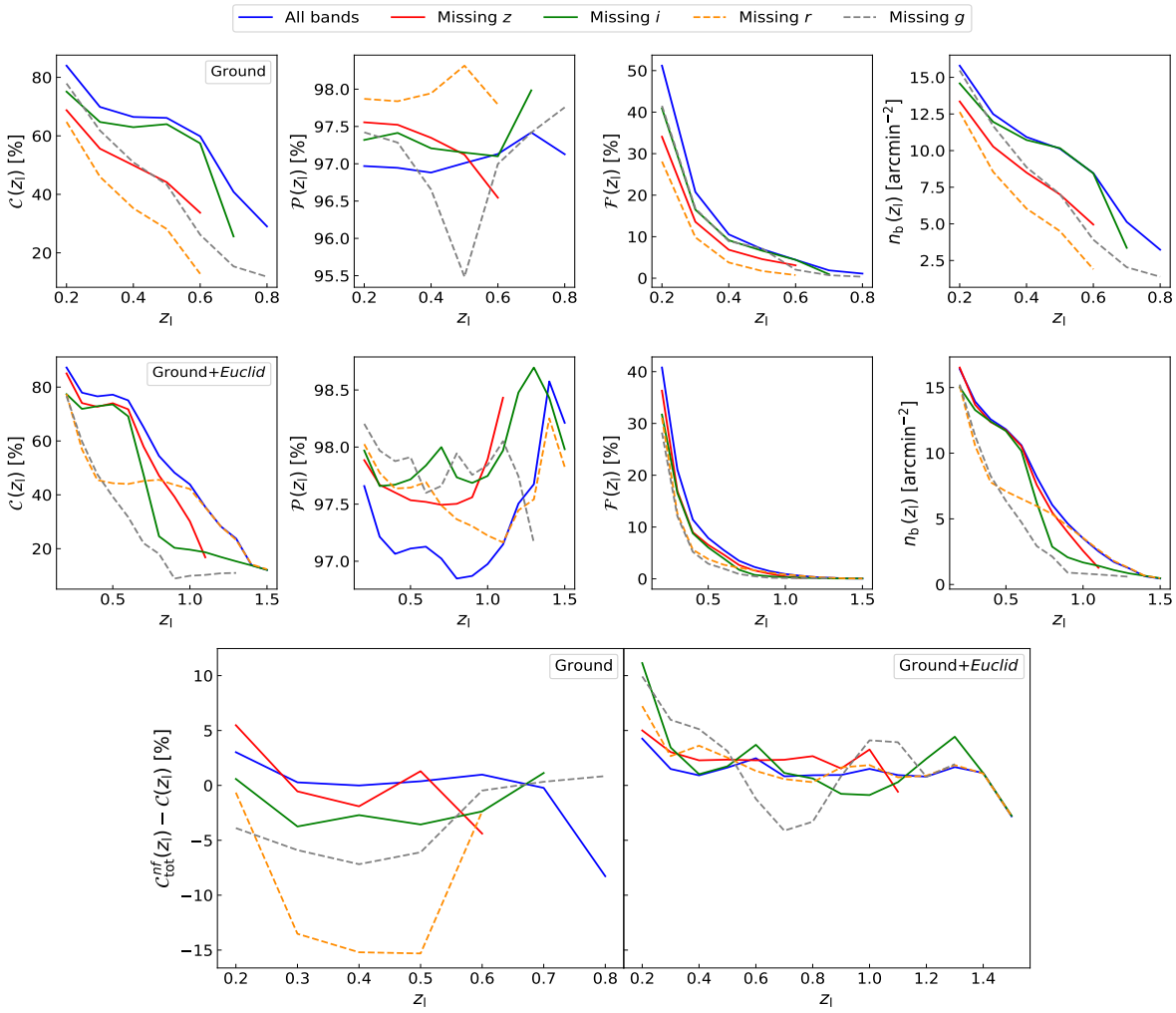

Fig. 10. Colour selection results, obtained from the B20 catalogue, in case of missing z (solid red), i (solid green), r (dashed orange), and g (dashed grey) bands. The blue curves represent the results from the *griz* and *griz*$Y_E J_E H_E$ selections reported in Tables A.1 and A.2. Top panels, from left to right: completeness, purity, foreground failure rate, and background density are shown, in the case of ground-only photometry. Middle panels: colour selections from the combination of ground-based and *Euclid* photometry. The plot structure is analogous to that of top panels. Bottom panels: difference between C^{nf}_{tot} and C, for ground-only observations (left panel) and for the combination of ground-based and *Euclid* photometry (right panel).

e.g. Jarvis et al. 2016; Melchior et al. 2017; Giblin et al. 2021). To assess the impact of colour selections on m, we considered the shape catalogues of Heymans et al. (2012), based on CFHTLS, and of Mandelbaum et al. (2018), based on the HSC Subaru Strategic Program (HSC-SSP; Miyazaki et al. 2018; Aihara et al. 2018). Throughout this section, we adopted a lens redshift of $z_l = 0.5$. By applying the *griz* selection calibrated in this work, we derived a shift in the mean shear multiplicative bias of $\Delta m = 7 \times 10^{-3}$ in CFHTLS and of $\Delta m = -2 \times 10^{-3}$ in HSC-SSP. In addition, the Oguri et al. (2012) and Medezinski et al. (2018) colour selections provide $\Delta m = -3 \times 10^{-3}$ and $\Delta m = -1 \times 10^{-2}$ from CFHTLS, respectively, while from HSC-SSP we obtained $\Delta m = -5 \times 10^{-3}$ and $\Delta m = -7 \times 10^{-3}$, respectively. Thus, galaxy population differences due to colour cuts provide systematic effects that are within the typical m uncertainty in stage III surveys. By combining colour and photo-z selections, we expect Δm to become closer to zero. In *Euclid*-like surveys, shear has to be calibrated within an accuracy of 2×10^{-3} (Cropper et al. 2013). As we discussed in Sect. 4.5, the combination of *griz*$Y_E J_E H_E$ and photo-z selections leads to 90% background completeness in the Euclid Wide Survey, on average; thus, we may expect the bias on m to be subdominant with respect to the required shear accuracy. Indeed, let us assume that 90% of galaxies, selected through the combination of *griz*$Y_E J_E H_E$ and photo-z selections, have an average m similar to that derived from stage III surveys, namely $\langle m \rangle = 0.01$. We assume that the remaining 10% of galaxies have a very biased m, namely $\langle m \rangle = 0.02$, compared to the selected population. This would imply a systematic error of $\Delta m = 10^{-3}$ in the average m of the selected population. We will delve deeper into these variations in m by examining the first data releases of the *Euclid* surveys.

4.7. Selection efficiency with missing bands

In this work, we derived colour selections based on *griz* and *griz*$Y_E J_E H_E$ photometry. In some cases, however, the full ground-based *griz* photometry may be not available. For example, the DES Year 3 galaxy shape catalogue was not based on g band (Gatti et al. 2021), due to issues in the point spread function estimation (Jarvis et al. 2021). Thus, we investigated the efficiency of *griz* and *griz*$Y_E J_E H_E$ selections in the case of a

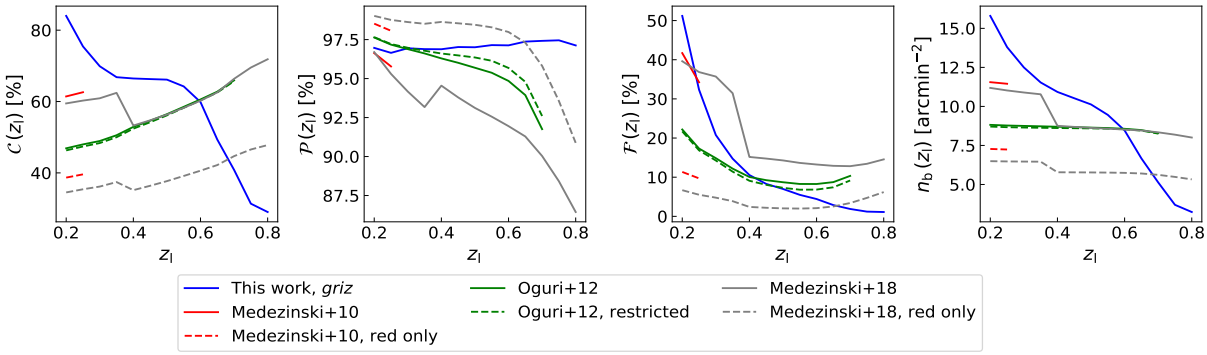

Fig. 11. Comparison of the *griz* selection described in Sect. 4.1 with literature colour selections. From left to right: completeness, purity, foreground failure rate, and background density, derived from the B20 catalogue. The blue solid lines represent the *griz* selection derived in this work. The red curves refer to the Medezinski et al. (2010) selection, where the solid lines are given by Eqs. (11)–(12), while the dashed lines are given by Eq. (11). The green curves represent the results from the Oguri et al. (2012) selection, where the solid lines are given by Eqs. (13)–(16), while the dashed lines are given by Eqs. (13)–(15). The grey curves refer to the Medezinski et al. (2018) selection, where the solid lines are given by Eqs. (17)–(18), while the dashed lines are given by Eq. (17).

missing band, based on the B20 calibration sample described in Sect. 2. In performing this test, we excluded the colour conditions in Tables A.1 and A.2 containing the chosen missing bands. In Fig. 10 we show that, in the case of ground-only observations, the absence of the r band implies the largest completeness decrease, providing $C(z_l) < 60\%$. In addition, the z_l range is substantially reduced, corresponding to $z_l \in [0.2, 0.6]$. Also the absence of i and z bands implies a reduction of the maximum z_l for the ground-based selection, corresponding to $z_l = 0.7$ and $z_l = 0.6$, respectively, and a completeness decrease of up to 10 and 20 percentage points, respectively. On average, a 20 percentage points drop in completeness is found in absence of g band photometry. Nevertheless, in the latter case the z_l range is not reduced. We remark that the considered samples differ from case to case, as they contain only galaxies with photometry available in the required bands.

In Fig. 10 we show the effect of missing photometric bands on the combination of ground-based and *Euclid* observations. In this case, the lack of r band does not imply changes in $C(z_l)$ for $z_l > 1$. In the absence of i band, $C(z_l)$ significantly decreases for $z_l \gtrsim 0.7$, being below 30%, while the z_l range is not reduced. A z_l range reduction is obtained in the case of missing z or g bands, as we derived $z_l \in [0.2, 1.1]$ and $z_l \in [0.2, 1.3]$, respectively. On average, in the case of the combination of ground-based and *Euclid* observations, the largest completeness decrease is caused by the lack of the g band.

In this section, we defined colour selections with missing g, r, i, or z band, as subsets of the colour conditions defining the *griz* and $grizY_EJ_EH_E$ selections. In order to assess the difference between the selections defined by such subsets and those that would be derived from the colour selection calibration described in Sect. 3, we compute C^{nf}_{tot} for each case. In Fig. 10, we show the difference between C^{nf}_{tot} and C, the latter being derived by subsets of the colour conditions defining *griz* and $grizY_EJ_EH_E$ selections. In the ground-only case, the lack of r band provides the largest C underestimation, as $C^{nf}_{tot} - C \sim 15$ percentage points for $z_l \in [0.3, 0.5]$. Nevertheless, in case of other missing bands, the average $C^{nf}_{tot} - C$ is close to 0. The same holds for the combination of ground-based and *Euclid* photometry. We conclude that *griz* and $grizY_EJ_EH_E$ selections provide robust results in the case of a missing band, except for ground-only observations without the r band, for which a dedicated calibration might be needed.

5. Comparison with literature ground-based selections

Based on the B20 sample considered in Sect. 4.1, we compared our *griz* colour selection to those derived by Medezinski et al. (2010, 2018) and Oguri et al. (2012), which are also implemented in `COMB-CL`. As detailed below, for each of these selections, we considered two versions. One includes all the colour conditions provided by the corresponding authors, while the other comprises only a subsample of such conditions, providing lower foreground contamination. `COMB-CL` includes both versions of each colour selection.

Medezinski et al. (2010) derived colour selections for three massive clusters, identified through deep Subaru imaging, by maximising their weak-lensing signal. `COMB-CL` provides the selection calibrated for the A1703 cluster at redshift $z_l \sim 0.26$, as this is the one based on *gri* photometry. This selection is expressed as follows,

$$[\,(g-r) < 2.17\,(r-i) - 0.37 \wedge (g-r) < -0.6\,(r-i) + 1.85 \wedge (r-i) > 0.3\,] \vee [\,(g-r) < -0.4\,(r-i) + 0.47 \wedge (r-i) < 0.3\,] \vee (r-i) < -0.06, \quad (11)$$

$$(r-i) < -0.06, \quad (12)$$

where $\wedge$ is the logical "and" operator. Notably, Eq. (11) defines the red background sample, namely the galaxies redder than cluster galaxies, while Eq. (12) defines the blue background sample. In Fig. 11, we can see that this selection provides $C(z_l) = 60\%$, which is 20 percentage points lower than that provided by the *griz* selection calibrated in this work. In addition, from the Medezinski et al. (2010) selection we derived $\mathcal{P}(z_l) > 96\%$, which is slightly lower than that obtained from the *griz* selection discussed in Sect. 4.1. Foreground contamination can be attenuated by considering the red sample selection only, namely Eq. (11), as shown in Fig. 11. In this case, however, the completeness is lowered by 20 percentage points. In Fig. 12 (upper panel), we show a comparison between the selection by Medezinski et al. (2010), namely Eqs. (11) and (12), and our *griz* selection in the $(r-i)-(g-r)$ colour-colour space, by assuming $z_l = 0.26$. Within this colour-colour space, we obtained $C(z_l) = 55\%$ and $\mathcal{P}(z_l) = 98\%$ from the *griz* selection, while through the Medezinski et al. (2010) selection we found $C(z_l) = 62\%$ and $\mathcal{P}(z_l) = 95\%$. We remark that the full set of colour conditions defining the *griz* selection yields 80%

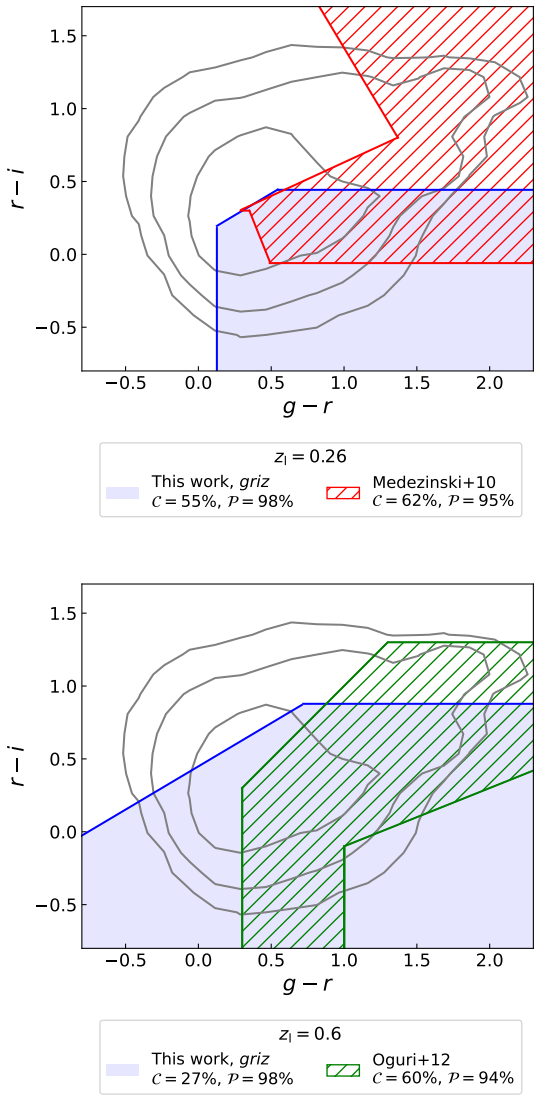

Fig. 12. Comparison of colour selections in the $(r-i)-(g-r)$ colour-colour space. The solid grey contours indicate the 68%, 95%, and 99% galaxy number density in the calibration sample, described in Sect. 2. The blue shaded areas represent the regions excluded by applying the *griz* selection calibrated in Sect. 4.1. Completeness and purity of the selections are reported in the legends. For the *griz* selection, C and $\mathcal{P}$ are computed by considering the colour conditions in Table A.1 which are defined in the $(r-i)-(g-r)$ space. Top panel: the red hatched area shows the region excluded through the Medezinski et al. (2010) selection, and $z_l = 0.26$ is assumed. Bottom panel: the green hatched area shows the region excluded through the Oguri et al. (2012) selection, and $z_l = 0.6$ is assumed.

completeness for $z_l = 0.26$, and that a calibration based on *gri* bands only would yield larger completeness values in the $(r-i)-(g-r)$ space (see Sect. 4.7). In addition, Fig. 12 shows that the *griz* selection extends the selected region defined by Eq. (11), thus enhancing the red background sample compared to Medezinski et al. (2010). On the other hand, the *griz* selection shows a more conservative definition of the blue background sample, compared to Eq. (12).

Oguri et al. (2012) calibrated a selection based on *gri* photometry from the COSMOS catalogue by Ilbert et al. (2009), providing reliable results for lenses at redshift $z_l \lesssim 0.7$. This selection is expressed as

$$(g-r) < 0.3 \vee \tag{13}$$
$$(r-i) > 1.3 \vee \tag{14}$$
$$(r-i) > (g-r) \vee \tag{15}$$
$$(g-r) > 1 \ \wedge \ (r-i) < 0.4\,(g-r) - 0.5. \tag{16}$$

The inclusion of Eq. (16) does not provide significant improvement in the completeness, causing a lower selection purity (Covone et al. 2014). In fact, Fig. 11 shows that the selection including Eqs. (13)–(16) provides sub-percent improvements in $C(z_l)$, compared to the selection including Eqs. (13)–(15) only, while $\mathcal{P}(z_l)$ and $\mathcal{F}(z_l)$ are up to 1 percentage point lower and higher, respectively. With respect to the *griz* selection calibrated in this work, the Oguri et al. (2012) selection provides a purity which is up to 5 percentage points lower. This explains the higher completeness values for $z_l > 0.6$. For lower z_l, the Oguri et al. (2012) selection provides a completeness up to 35 percentage points lower, which is expected as the selection by Oguri et al. (2012) was calibrated for clusters at $z_l \sim 0.7$. Similarly to the comparison with the Medezinski et al. (2010) selection discussed above, in Fig. 12 (lower panel) we compare the *griz* and Oguri et al. (2012) selections in the $(r-i)-(g-r)$ colour-colour space, assuming $z_l = 0.6$. We obtained $C(z_l) = 27\%$ and $\mathcal{P}(z_l) = 98\%$ from the *griz* selection, while with the Oguri et al. (2012) selection we found $C(z_l) = 60\%$ and $\mathcal{P}(z_l) = 94\%$. With respect to what we found by comparing *griz* and Medezinski et al. (2010) selections at $z_l = 0.26$, the decrease in completeness due to a purity enhancement is much larger at $z_l = 0.6$. This depends on the overlap of the foreground and background galaxy distributions in the $(r-i)-(g-r)$ space. In addition, we remark that the calibration process presented in Sect. 3 excludes redundant colour conditions. This may partially explain the 27% completeness found in the case of the *griz* selection.

Medezinski et al. (2018) calibrated a colour selection based on HSC observations, including *griz* bands, following an approach similar to Medezinski et al. (2010). This colour selection is expressed as

$$\Bigg[(g-i) < 2.276\,(r-z) - 0.152 + a(z_l) \ \wedge$$
$$(g-i) < \frac{1}{2.276}\,(r-z) + b(z_l)\left(1 + \frac{1}{2.276^2}\right) - \frac{0.152}{2.276^2} \ \wedge$$
$$(r-z) > 0.5 \ \wedge$$
$$z > 21\Bigg] \vee \tag{17}$$

$$\Bigg\{(r-z) < -0.0248\,z + 1.604 + c(z_l) \ \vee$$
$$\Bigg[(g-i) < \frac{1}{2.276}\,(r-z) + d(z_l)\left(1 + \frac{1}{2.276^2}\right) - \frac{0.152}{2.276^2} \ \wedge$$
$$(g-i) < 4\Bigg] \vee$$
$$(r-z) < 0.5 \ \vee$$
$$z > 22\Bigg\}, \tag{18}$$

where

$$a(z_l) = \begin{cases} -0.7 & \text{if } z_l < 0.4 \\ -0.8 & \text{if } z_l \geq 0.4, \end{cases} \tag{19}$$

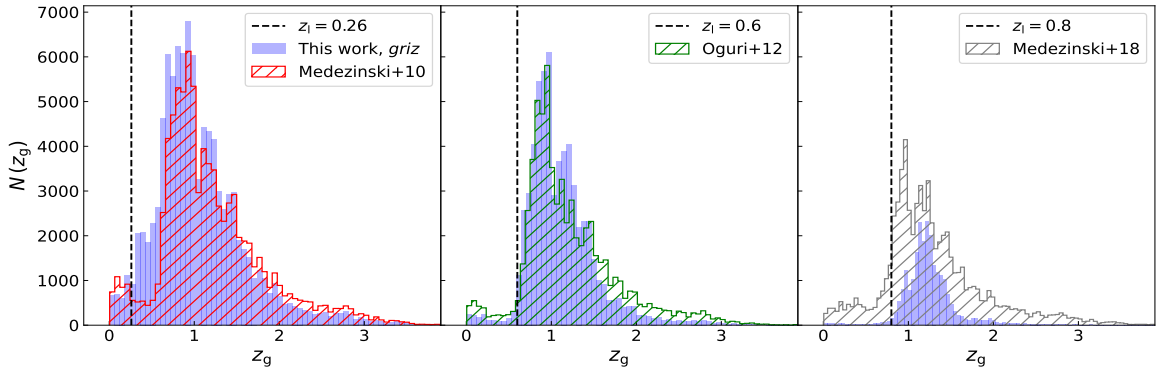

Fig. 13. From left to right: number of selected galaxies as a function of z_g assuming $z_l = 0.26$, $z_l = 0.6$, and $z_l = 0.8$. The z_l values are represented by vertical black dashed lines. The blue histograms represent the *griz* selection calibrated in this work. The galaxy redshift distributions derived with the Medezinski et al. (2010, 2018) and Oguri et al. (2012), selections are represented by red, green, and grey hatched histograms, respectively.

$$b(z_l) = \begin{cases} 4.0 & \text{if } z_l < 0.4 \\ 1.7 & \text{if } z_l \geq 0.4, \end{cases} \tag{20}$$

$$c(z_l) = \begin{cases} -0.8 & \text{if } z_l < 0.4 \\ -0.9 & \text{if } z_l \geq 0.4, \end{cases} \tag{21}$$

$$d(z_l) = \begin{cases} 0.5 & \text{if } z_l < 0.4 \\ 0.3 & \text{if } z_l \geq 0.4. \end{cases} \tag{22}$$

Similarly to Medezinski et al. (2010), Eqs. (17) and (18) define the red and blue background samples, respectively. This selection provides a much larger amount of contamination compared to that derived in this work, reaching $\mathcal{P}(z_l) < 90\%$ for $z_l > 0.7$, as shown in Fig. 11. However, by considering the red sample selection only, the purity improves by up to 6 percentage points. In the latter case, compared to the *griz* selection detailed in Table A.1, $C(z_l)$ is up to 50 percentage points lower for $z_l < 0.7$. For higher z_l, the lower purity from the Medezinski et al. (2018) selection allows for higher completeness values.

In Fig. 13 we show the redshift distributions of the galaxies selected through the *griz*, Medezinski et al. (2010, 2018) and Oguri et al. (2012) selections, assuming different z_l values. At $z_l = 0.26$, the *griz* selection shows a larger number of galaxies, of the order of 10^3, which are correctly identified as background objects with $z_g < 0.6$, compared to Medezinski et al. (2010). This results in the larger completeness of the *griz* selection shown in Fig. 11. At $z_l = 0.6$, where the *griz* and Oguri et al. (2012) selections have the same completeness (see Fig. 11), the *griz* selection is less complete at $z_g > 1.5$ and more complete at lower redshifts, compared to Oguri et al. (2012). At $z_l = 0.8$, where the *griz* selection is remarkably purer than that by Medezinski et al. (2018), a notable incompleteness of the *griz* selection is evident at any z_g, compared to Medezinski et al. (2018). In fact, for the case of the *griz* selection, Fig. 13 shows that the number of rejected galaxies at high redshift increases with the number of excluded foreground galaxies. This reflects the overlapping of foreground and background galaxy distributions in the considered colour-colour spaces.

6. Discussion and conclusions

We developed a method to derive optimal galaxy colour selections for cluster weak-lensing analyses, given any set of photometric bands. To this aim, we considered all the available colour-colour combinations. Based on the galaxy catalogue by B20, we calibrated selections based on ground-based *griz* and *Euclid* $Y_E J_E H_E$ bands, with purity higher than 97%. Specifically, we showed that the *griz* selection provides a completeness between 30% and 84%, in the lens limiting redshift range $z_l \in [0.2, 0.8]$. The inclusion of *Euclid* $Y_E J_E H_E$ bands, leading to a $griz Y_E J_E H_E$ selection, improves the completeness by up to 25 percentage points in this z_l range, allowing for a galaxy selection up to $z_l = 1.5$. In addition, for the first time in the literature, we expressed such selections as a continuous function of z_l. In the following, we summarise the main results obtained from the tests presented in Sects. 4 and 5.

- The calibrated colour selections, described in Sect. 4.1, are stable with respect to changes in the sample limiting magnitudes and redshift.
- By applying the *griz* selection to the VMLS catalogue by Moutard et al. (2016) and to the COSMOS20 catalogue by Weaver et al. (2022), we derived completeness and purity estimates that are consistent with those obtained from the calibration sample by B20. Consequently, the calibrated selections provide stable results by assuming alternative photometric aperture definitions, obtained from different ground-based telescopes.
- The application of *griz* and $griz Y_E J_E H_E$ selections to the simulated *Euclid* Flagship galaxy catalogue v2.1.10 (Euclid Collaboration, in prep.) provided a purity of around 99%, on average, which is higher than that obtained from the B20 catalogue. The completeness from the Flagship and B20 samples is compatible in the *griz* selection case, while the $griz Y_E J_E H_E$ selection provides up to 50 percentage points higher completeness from Flagship. We verified that this discrepancy does not depend on magnitude limits. In addition, we found no significant differences in the star forming galaxy fraction from the Flagship and B20 samples. A calibration of the $griz Y_E J_E H_E$ selection based on the *Euclid* Deep Survey will allow for a more thorough investigation of these completeness differences.
- Based on the Flagship sample, we combined the calibrated colour selections with photo-z selections based on the $p(z_g)$ shape. We showed that in this case the completeness is up to 95%.
- We found no significant systematic effects on the multiplicative shear bias due to colour selections for stage III surveys. The first *Euclid* data releases will provide further insights into the influence of background selections on this bias.
- The calibrated colour selections provide robust results in the case of a missing band from ground-based observations,

except for those without the r band, for which a dedicated calibration might be needed.
– Compared to the ground-based colour selections provided by Medezinski et al. (2010, 2018) and Oguri et al. (2012), the *griz* selection derived in this work is purer at high redshift and more complete at low redshift.

One potential enhancement to the calibration presented in this work could entail the inclusion of a magnitude dependence in the colour cuts. This might mitigate the impact of large photometric scatter at faint magnitudes (see, e.g. Schrabback et al. 2021). In addition, enhancing the set of photometric bands in the calibration sample, for example by including the LSST y band, could remarkably improve the effectiveness of the colour selections. The performance of colour selections could further improve through dedicated calibration samples. Ongoing spectroscopic programmes are specifically designed to calibrate the relationship between galaxy colours and redshifts to match the depth of the *Euclid* survey (Euclid Collaboration 2022c).

Furthermore, the colour selections presented in this work could improve the shear calibration in cluster weak-lensing analyses. The lensing signal from galaxy clusters differs from that of large scale structure in ways that affect both shear and photometric measurements. The dense cluster environment causes increased blending among light sources, due to both galaxy blends (Simet & Mandelbaum 2015; Everett et al. 2022) and the presence of diffuse intra-cluster light (Gruen et al. 2019; Kluge et al. 2020; Sampaio-Santos et al. 2021). In addition, cluster lines of sight exhibit characteristically stronger shear, especially at small scales (McClintock et al. 2019; Ingoglia et al. 2022). These effects can lead to distinct biases in shear measurements compared to those obtained from calibrations primarily designed for cosmic shear analyses. Through the combination of colour and photo-z selections, cluster shear calibration and mass bias can be assessed based on dedicated, multi-band cluster image simulations (see, e.g. Hernández-Martín et al. 2020).

Acknowledgements. The *Euclid* Consortium acknowledges the European Space Agency and a number of agencies and institutes that have supported the development of *Euclid*, in particular the Academy of Finland, the Agenzia Spaziale Italiana, the Belgian Science Policy, the Canadian *Euclid* Consortium, the French Centre National d'Etudes Spatiales, the Deutsches Zentrum für Luft- und Raumfahrt, the Danish Space Research Institute, the Fundação para a Ciência e a Tecnologia, the Ministerio de Ciencia e Innovación, the National Aeronautics and Space Administration, the National Astronomical Observatory of Japan, the Netherlandse Onderzoekschool Voor Astronomie, the Norwegian Space Agency, the Romanian Space Agency, the State Secretariat for Education, Research and Innovation (SERI) at the Swiss Space Office (SSO), and the United Kingdom Space Agency. A complete and detailed list is available on the *Euclid* website (https://www.euclid-ec.org) We thank W. Hartley for his valuable advice, which remarkably enhanced the quality of this work. G.C. and L.M. acknowledge the support from the grant ASI n.2018-23-HH.0. L.M. and F.M. acknowledge the financial contribution from the grant PRIN-MUR 2022 20227RNLY3 "The concordance cosmological model: stress-tests with galaxy clusters" supported by Next Generation EU. L.B. acknowledges financial support from PRIN-MIUR 2017–20173ML3WW_001. M.S. acknowledges financial contributions from contract ASI-INAF n.2017-14-H.0, contract INAF mainstream project 1.05.01.86.10, and INAF Theory Grant 2023: Gravitational lensing detection of matter distribution at galaxy cluster boundaries and beyond (1.05.23.06.17). G.C. thanks the support from INAF Theory Grant 2022: Illuminating Dark Matter using Weak Lensing by Cluster Satellites, PI: Carlo Giocoli. This work has made use of CosmoHub (Carretero et al. 2017; Tallada et al. 2020). CosmoHub has been developed by the Port d'Informació Científica (PIC), maintained through a collaboration of the Institut de Física d'Altes Energies (IFAE) and the Centro de Investigaciones Energéticas, Medioambientales y Tecnológicas (CIEMAT) and the Institute of Space Sciences (CSIC & IEEC), and was partially funded by the "Plan Estatal de Investigación Científica y Técnica y de Innovación" program of the Spanish government.

References

Abbott, T. M. C., Aguena, M., Alarcon, A., et al. 2020, Phys. Rev. D, 102, 023509
Aihara, H., Armstrong, R., Bickerton, S., et al. 2018, PASJ, 70, S8
Applegate, D. E., von der Linden, A., Kelly, P. L., et al. 2014, MNRAS, 439, 48
Baltz, E. A., Marshall, P., & Oguri, M. 2009, JCAP, 2009, 015
Behroozi, P. S., Wechsler, R. H., & Wu, H.-Y. 2013, ApJ, 762, 109
Bellagamba, F., Sereno, M., Roncarelli, M., et al. 2019, MNRAS, 484, 1598
Bisigello, L., Kuchner, U., Conselice, C. J., et al. 2020, MNRAS, 494, 2337
Broadhurst, T., Takada, M., Umetsu, K., et al. 2005, ApJ, 619, L143
Bruzual, G., & Charlot, S. 2003, MNRAS, 344, 1000
Carretero, J., Tallada, P., Casals, J., et al. 2017, Proceedings of the European Physical Society Conference on High Energy Physics, 5-12 July, 488
Chambers, K. C., Magnier, E. A., Metcalfe, N., et al. 2016, arXiv e-prints [arXiv:1612.05560]
CHEX-MATE Collaboration (Arnaud, M., et al.) 2021, A&A, 650, A104
Costanzi, M., Rozo, E., Simet, M., et al. 2019, MNRAS, 488, 4779
Covone, G., Sereno, M., Kilbinger, M., & Cardone, V. F. 2014, ApJ, 784, L25
Cropper, M., Hoekstra, H., Kitching, T., et al. 2013, MNRAS, 431, 3103
Cropper, M., Pottinger, S., Niemi, S., et al. 2016, in Space Telescopes and Instrumentation 2016: Optical, Infrared, and Millimeter Wave, eds. H. A. MacEwen, G. G. Fazio, M. Lystrup, et al., SPIE Conf. Ser., 9904, 99040Q
Diemer, B., & Kravtsov, A. V. 2014, ApJ, 789, 1
Dietrich, J. P., Bocquet, S., Schrabback, T., et al. 2019, MNRAS, 483, 2871
Eckert, D., Ettori, S., Robertson, A., et al. 2022, A&A, 666, A41
Euclid Collaboration (Adam, R., et al.) 2019, A&A, 627, A23
Euclid Collaboration (Desprez, G., et al.) 2020, A&A, 644, A31
Euclid Collaboration (Pocino, A., et al.) 2021, A&A, 655, A44
Euclid Collaboration (Scaramella, R., et al.) 2022a, A&A, 662, A112
Euclid Collaboration (Schirmer, M., et al.) 2022b, A&A, 662, A92
Euclid Collaboration (Saglia, R., et al.) 2022c, A&A, 664, A196
Euclid Collaboration (Bisigello, L., et al.) 2023a, MNRAS, 520, 3529
Euclid Collaboration (Sereno, M., et al.) 2023b, A&A, submitted
Everett, S., Yanny, B., Kuropatkin, N., et al. 2022, ApJS, 258, 15
Gatti, M., Sheldon, E., Amon, A., et al. 2021, MNRAS, 504, 4312
Giblin, B., Heymans, C., Asgari, M., et al. 2021, A&A, 645, A105
Gruen, D., Seitz, S., Brimioulle, F., et al. 2014, MNRAS, 442, 1507
Gruen, D., Zhang, Y., Palmese, A., et al. 2019, MNRAS, 488, 4389
Gunn, J. E., Carr, M., Rockosi, C., et al. 1998, AJ, 116, 3040
Guzzo, L., Scodeggio, M., Garilli, B., et al. 2014, A&A, 566, A108
Gwyn, S. D. J. 2012, AJ, 143, 38
Hernández-Martín, B., Schrabback, T., Hoekstra, H., et al. 2020, A&A, 640, A117
Heymans, C., & Heavens, A. 2003, MNRAS, 339, 711
Heymans, C., Van Waerbeke, L., Miller, L., et al. 2012, MNRAS, 427, 146
Hildebrandt, H., Choi, A., Heymans, C., et al. 2016, MNRAS, 463, 635
Hoekstra, H., Mahdavi, A., Babul, A., & Bildfell, C. 2012, MNRAS, 427, 1298
Hudelot, P., Cuillandre, J. C., Withington, K., et al. 2012, VizieR Online Data Catalog: II/317
Ibata, R. A., McConnachie, A., Cuillandre, J.-C., et al. 2017, ApJ, 848, 128
Ilbert, O., Capak, P., Salvato, M., et al. 2009, ApJ, 690, 1236
Ingoglia, L., Covone, G., Sereno, M., et al. 2022, MNRAS, 511, 1484
Ivezic, Z., Axelrod, T., Brandt, W. N., et al. 2008, Serb. Astron. J., 176, 1
Iye, M., Karoji, H., Ando, H., et al. 2004, PASJ, 56, 381
Jarvis, M., Sheldon, E., Zuntz, J., et al. 2016, MNRAS, 460, 2245
Jarvis, M., Bernstein, G. M., Amon, A., et al. 2021, MNRAS, 501, 1282
Klein, M., Israel, H., Nagarajan, A., et al. 2019, MNRAS, 488, 1704
Kluge, M., Neureiter, B., Riffeser, A., et al. 2020, ApJS, 247, 43
Kron, R. G. 1980, ApJS, 43, 305
Kuijken, K., Heymans, C., Dvornik, A., et al. 2019, A&A, 625, A2
Laigle, C., McCracken, H. J., Ilbert, O., et al. 2016, ApJS, 224, 24
Laureijs, R., Amiaux, J., Arduini, S., et al. 2011, arXiv e-prints [arXiv:1110.3193]
Lesci, G. F., Marulli, F., Moscardini, L., et al. 2022, A&A, 659, A88
Li, X., Miyatake, H., Luo, W., et al. 2022, PASJ, 74, 421
Mandelbaum, R., Miyatake, H., Hamana, T., et al. 2018, PASJ, 70, S25
Mantz, A. B., von der Linden, A., Allen, S. W., et al. 2015, MNRAS, 446, 2205
Marulli, F., Veropalumbo, A., García-Farieta, J. E., et al. 2021, ApJ, 920, 13
Maturi, M., Bellagamba, F., Radovich, M., et al. 2019, MNRAS, 485, 498
McClintock, T., Varga, T. N., Gruen, D., et al. 2019, MNRAS, 482, 1352
Medezinski, E., Broadhurst, T., Umetsu, K., et al. 2007, ApJ, 663, 717
Medezinski, E., Broadhurst, T., Umetsu, K., et al. 2010, MNRAS, 405, 257
Medezinski, E., Oguri, M., Nishizawa, A. J., et al. 2018, PASJ, 70, 30
Melchior, P., Suchyta, E., Huff, E., et al. 2015, MNRAS, 449, 2219
Melchior, P., Gruen, D., McClintock, T., et al. 2017, MNRAS, 469, 4899
Miller, L., Heymans, C., Kitching, T. D., et al. 2013, MNRAS, 429, 2858
Miyazaki, S., Komiyama, Y., Kawanomoto, S., et al. 2018, PASJ, 70, S1

Moutard, T., Arnouts, S., Ilbert, O., et al. 2016, A&A, 590, A102
Navarro, J. F., Frenk, C. S., & White, S. D. M. 1997, ApJ, 490, 493
Oguri, M., Bayliss, M. B., Dahle, H., et al. 2012, MNRAS, 420, 3213
Okabe, N., Zhang, Y. Y., Finoguenov, A., et al. 2010, ApJ, 721, 875
Peter, A. H. G., Rocha, M., Bullock, J. S., & Kaplinghat, M. 2013, MNRAS, 430, 105
Planck Collaboration XXIV. 2016, A&A, 594, A24
Polletta, M., Tajer, M., Maraschi, L., et al. 2007, ApJ, 663, 81
Pratt, G. W., Arnaud, M., Biviano, A., et al. 2019, Space Sci. Rev., 215, 25
Robertson, A., Massey, R., & Eke, V. 2017, MNRAS, 465, 569
Rykoff, E. S., Rozo, E., Hollowood, D., et al. 2016, ApJS, 224, 1
Sampaio-Santos, H., Zhang, Y., Ogando, R. L. C., et al. 2021, MNRAS, 501, 1300
Schrabback, T., Schirmer, M., van der Burg, R. F. J., et al. 2018, A&A, 610, A85
Schrabback, T., Bocquet, S., Sommer, M., et al. 2021, MNRAS, 505, 3923
Sereno, M., Veropalumbo, A., Marulli, F., et al. 2015, MNRAS, 449, 4147
Sereno, M., Covone, G., Izzo, L., et al. 2017, MNRAS, 472, 1946
Sereno, M., Lovisari, L., Cui, W., & Schellenberger, G. 2021, MNRAS, 507, 5214
Sevilla-Noarbe, I., Bechtol, K., Carrasco Kind, M., et al. 2021, ApJS, 254, 24
Sifón, C., Hoekstra, H., Cacciato, M., et al. 2015, A&A, 575, A48
Simet, M., & Mandelbaum, R. 2015, MNRAS, 449, 1259
Stern, C., Dietrich, J. P., Bocquet, S., et al. 2019, MNRAS, 485, 69
Tallada, P., Carretero, J., Casals, J., et al. 2020, Astron. Comput., 32, 32
Teyssier, R., Moore, B., Martizzi, D., Dubois, Y., & Mayer, L. 2011, MNRAS, 414, 195
Umetsu, K. 2020, A&ARv, 28, 7
Vazza, F., Jones, T. W., Brüggen, M., et al. 2017, MNRAS, 464, 210
Weaver, J. R., Kauffmann, O. B., Ilbert, O., et al. 2022, ApJS, 258, 11
Zhu, Z., Xu, H., Hu, D., et al. 2021, ApJ, 908, 17
Zohren, H., Schrabback, T., Bocquet, S., et al. 2022, A&A, 668, A18

[1] Dipartimento di Fisica e Astronomia "Augusto Righi" – Alma Mater Studiorum Università di Bologna, Via Piero Gobetti 93/2, 40129 Bologna, Italy
e-mail: giorgio.lesci2@unibo.it
[2] INAF-Osservatorio di Astrofisica e Scienza dello Spazio di Bologna, Via Piero Gobetti 93/3, 40129 Bologna, Italy
[3] INFN-Sezione di Bologna, Viale Berti Pichat 6/2, 40127 Bologna, Italy
[4] INAF-Osservatorio Astronomico di Padova, Via dell'Osservatorio 5, 35122 Padova, Italy
[5] Dipartimento di Fisica e Astronomia "G. Galilei", Università di Padova, Via Marzolo 8, 35131 Padova, Italy
[6] Université Paris-Saclay, Université Paris Cité, CEA, CNRS, AIM, 91191 Gif-sur-Yvette, France
[7] Department of Physics "E. Pancini", University Federico II, Via Cinthia 6, 80126 Napoli, Italy
[8] INAF-Osservatorio Astronomico di Capodimonte, Via Moiariello 16, 80131 Napoli, Italy
[9] INFN Section of Naples, Via Cinthia 6, 80126 Napoli, Italy
[10] Istituto Nazionale di Fisica Nucleare, Sezione di Bologna, Via Irnerio 46, 40126 Bologna, Italy
[11] Université Côte d'Azur, Observatoire de la Côte d'Azur, CNRS, Laboratoire Lagrange, Bd de l'Observatoire, CS 34229, 06304 Nice Cedex 4, France
[12] INAF-Osservatorio Astronomico di Trieste, Via G. B. Tiepolo 11, 34143 Trieste, Italy
[13] IFPU, Institute for Fundamental Physics of the Universe, Via Beirut 2, 34151 Trieste, Italy
[14] Université Paris-Saclay, CNRS, Institut d'Astrophysique Spatiale, 91405 Orsay, France
[15] Institute of Cosmology and Gravitation, University of Portsmouth, Portsmouth PO1 3FX, UK
[16] INAF-Osservatorio Astronomico di Brera, Via Brera 28, 20122 Milano, Italy
[17] Dipartimento di Fisica e Astronomia, Università di Bologna, Via Gobetti 93/2, 40129 Bologna, Italy
[18] Max Planck Institute for Extraterrestrial Physics, Giessenbachstr. 1, 85748 Garching, Germany
[19] Universitäts-Sternwarte München, Fakultät für Physik, Ludwig-Maximilians-Universität München, Scheinerstrasse 1, 81679 München, Germany
[20] INAF-Osservatorio Astrofisico di Torino, Via Osservatorio 20, 10025 Pino Torinese, TO, Italy
[21] Dipartimento di Fisica, Università di Genova, Via Dodecaneso 33, 16146 Genova, Italy
[22] INFN-Sezione di Genova, Via Dodecaneso 33, 16146 Genova, Italy
[23] Instituto de Astrofísica e Ciências do Espaço, Universidade do Porto, CAUP, Rua das Estrelas, 4150-762 Porto, Portugal
[24] Dipartimento di Fisica, Università degli Studi di Torino, Via P. Giuria 1, 10125 Torino, Italy
[25] INFN-Sezione di Torino, Via P. Giuria 1, 10125 Torino, Italy
[26] INAF-IASF Milano, Via Alfonso Corti 12, 20133 Milano, Italy
[27] Institut de Física d'Altes Energies (IFAE), The Barcelona Institute of Science and Technology, Campus UAB, 08193 Bellaterra, Barcelona, Spain
[28] Port d'Informació Científica, Campus UAB, C. Albareda s/n, 08193 Bellaterra, Barcelona, Spain
[29] Institute for Theoretical Particle Physics and Cosmology (TTK), RWTH Aachen University, 52056 Aachen, Germany
[30] Institute of Space Sciences (ICE, CSIC), Campus UAB, Carrer de Can Magrans, s/n, 08193 Barcelona, Spain
[31] Institut d'Estudis Espacials de Catalunya (IEEC), Carrer Gran Capitá 2-4, 08034 Barcelona, Spain
[32] INAF-Osservatorio Astronomico di Roma, Via Frascati 33, 00078 Monteporzio Catone, Italy
[33] Dipartimento di Fisica e Astronomia "Augusto Righi" – Alma Mater Studiorum Università di Bologna, Viale Berti Pichat 6/2, 40127 Bologna, Italy
[34] Institute for Astronomy, University of Edinburgh, Royal Observatory, Blackford Hill, Edinburgh EH9 3HJ, UK
[35] Jodrell Bank Centre for Astrophysics, Department of Physics and Astronomy, University of Manchester, Oxford Road, Manchester M13 9PL, UK
[36] European Space Agency/ESRIN, Largo Galileo Galilei 1, 00044 Frascati, Roma, Italy
[37] ESAC/ESA, Camino Bajo del Castillo, s/n, Urb. Villafranca del Castillo, 28692 Villanueva de la Cañada, Madrid, Spain
[38] University of Lyon, Univ. Claude Bernard Lyon 1, CNRS/IN2P3, IP2I Lyon, UMR 5822, 69622 Villeurbanne, France
[39] Institute of Physics, Laboratory of Astrophysics, Ecole Polytechnique Fédérale de Lausanne (EPFL), Observatoire de Sauverny, 1290 Versoix, Switzerland
[40] UCB Lyon 1, CNRS/IN2P3, IUF, IP2I Lyon, 4 Rue Enrico Fermi, 69622 Villeurbanne, France
[41] Departamento de Física, Faculdade de Ciências, Universidade de Lisboa, Edifício C8, Campo Grande, 1749-016 Lisboa, Portugal
[42] Instituto de Astrofísica e Ciências do Espaço, Faculdade de Ciências, Universidade de Lisboa, Campo Grande, 1749-016 Lisboa, Portugal
[43] Department of Astronomy, University of Geneva, Ch. d'Ecogia 16, 1290 Versoix, Switzerland
[44] INAF-Istituto di Astrofisica e Planetologia Spaziali, Via del Fosso del Cavaliere, 100, 00100 Roma, Italy
[45] Department of Physics, Oxford University, Keble Road, Oxford OX1 3RH, UK
[46] INFN-Padova, Via Marzolo 8, 35131 Padova, Italy
[47] Institut de Ciencies de l'Espai (IEEC-CSIC), Campus UAB, Carrer de Can Magrans, s/n Cerdanyola del Vallés, 08193 Barcelona, Spain
[48] School of Physics, HH Wills Physics Laboratory, University of Bristol, Tyndall Avenue, Bristol BS8 1TL, UK
[49] University Observatory, Faculty of Physics, Ludwig-Maximilians-Universität, Scheinerstr. 1, 81679 Munich, Germany
[50] Institute of Theoretical Astrophysics, University of Oslo, PO Box 1029, Blindern 0315, Oslo, Norway

[51] Department of Physics, Lancaster University, Lancaster LA1 4YB, UK
[52] von Hoerner & Sulger GmbH, SchloßPlatz 8, 68723 Schwetzingen, Germany
[53] Technical University of Denmark, Elektrovej 327, 2800 Kgs. Lyngby, Denmark
[54] Cosmic Dawn Center (DAWN), Copenhagen, Denmark
[55] Institut d'Astrophysique de Paris, UMR 7095, CNRS, and Sorbonne Université, 98 bis boulevard Arago, 75014 Paris, France
[56] Max-Planck-Institut für Astronomie, Königstuhl 17, 69117 Heidelberg, Germany
[57] Aix-Marseille Université, CNRS/IN2P3, CPPM, Marseille, France
[58] Jet Propulsion Laboratory, California Institute of Technology, 4800 Oak Grove Drive, Pasadena, CA 91109, USA
[59] AIM, CEA, CNRS, Université Paris-Saclay, Université de Paris, 91191 Gif-sur-Yvette, France
[60] Université de Genève, Département de Physique Théorique and Centre for Astroparticle Physics, 24 Quai Ernest-Ansermet, 1211 Genève 4, Switzerland
[61] Department of Physics, University of Helsinki, PO Box 64, 00014 Helsinki, Finland
[62] Helsinki Institute of Physics, University of Helsinki, Gustaf Hällströmin katu 2, Helsinki, Finland
[63] NOVA Optical Infrared Instrumentation Group at ASTRON, Oude Hoogeveensedijk 4, 7991 PD Dwingeloo, The Netherlands
[64] Universität Bonn, Argelander-Institut für Astronomie, Auf dem Hügel 71, 53121 Bonn, Germany
[65] Aix-Marseille Université, CNRS, CNES, LAM, Marseille, France
[66] Department of Physics, Institute for Computational Cosmology, Durham University, South Road, DH1 3LE Durham, UK
[67] University of Applied Sciences and Arts of Northwestern Switzerland, School of Engineering, 5210 Windisch, Switzerland
[68] Institut d'Astrophysique de Paris, 98bis Boulevard Arago, 75014 Paris, France
[69] European Space Agency/ESTEC, Keplerlaan 1, 2201 AZ Noordwijk, The Netherlands
[70] Department of Physics and Astronomy, University of Aarhus, Ny Munkegade 120, 8000 Aarhus C, Denmark
[71] Université Paris-Saclay, Université Paris Cité, CEA, CNRS, Astrophysique, Instrumentation et Modélisation Paris-Saclay, 91191 Gif-sur-Yvette, France
[72] Space Science Data Center, Italian Space Agency, Via del Politecnico snc, 00133 Roma, Italy
[73] Centre National d'Etudes Spatiales – Centre Spatial de Toulouse, 18 Avenue Edouard Belin, 31401 Toulouse Cedex 9, France
[74] Institute of Space Science, Str. Atomistilor, nr. 409 Măgurele, Ilfov 077125, Romania
[75] Instituto de Astrofísica de Canarias, Calle Vía Láctea s/n, 38204 San Cristóbal de La Laguna, Tenerife, Spain
[76] Departamento de Astrofísica, Universidad de La Laguna, 38206 La Laguna, Tenerife, Spain
[77] Departamento de Física, FCFM, Universidad de Chile, Blanco Encalada 2008, Santiago, Chile
[78] Satlantis, University Science Park, Sede Bld, 48940 Leioa-Bilbao, Spain
[79] Centre for Electronic Imaging, Open University, Walton Hall, Milton Keynes MK7 6AA, UK
[80] Centro de Investigaciones Energéticas, Medioambientales y Tecnológicas (CIEMAT), Avenida Complutense 40, 28040 Madrid, Spain
[81] Infrared Processing and Analysis Center, California Institute of Technology, Pasadena, CA 91125, USA
[82] Instituto de Astrofísica e Ciências do Espaço, Faculdade de Ciências, Universidade de Lisboa, Tapada da Ajuda, 1349-018 Lisboa, Portugal
[83] Universidad Politécnica de Cartagena, Departamento de Electrónica y Tecnología de Computadoras, Plaza del Hospital 1, 30202 Cartagena, Spain
[84] Institut de Recherche en Astrophysique et Planétologie (IRAP), Université de Toulouse, CNRS, UPS, CNES, 14 Av. Edouard Belin, 31400 Toulouse, France
[85] Kapteyn Astronomical Institute, University of Groningen, PO Box 800, 9700 AV Groningen, The Netherlands
[86] INFN-Bologna, Via Irnerio 46, 40126 Bologna, Italy
[87] Department of Mathematics and Physics E. De Giorgi, University of Salento, Via per Arnesano, CP-I93, 73100 Lecce, Italy
[88] INAF-Sezione di Lecce, c/o Dipartimento Matematica e Fisica, Via per Arnesano, 73100 Lecce, Italy
[89] INFN, Sezione di Lecce, Via per Arnesano, CP-193, 73100 Lecce, Italy
[90] Institut für Theoretische Physik, University of Heidelberg, Philosophenweg 16, 69120 Heidelberg, Germany
[91] Université St Joseph; Faculty of Sciences, Beirut, Lebanon
[92] Junia, EPA department, 41 Bd Vauban, 59800 Lille, France
[93] SISSA, International School for Advanced Studies, Via Bonomea 265, 34136 Trieste, TS, Italy
[94] INFN, Sezione di Trieste, Via Valerio 2, 34127 Trieste, TS, Italy
[95] ICSC – Centro Nazionale di Ricerca in High Performance Computing, Big Data e Quantum Computing, Via Magnanelli 2, Bologna, Italy
[96] Instituto de Física Teórica UAM-CSIC, Campus de Cantoblanco, 28049 Madrid, Spain
[97] CERCA/ISO, Department of Physics, Case Western Reserve University, 10900 Euclid Avenue, Cleveland, OH 44106, USA
[98] Laboratoire Univers et Théorie, Observatoire de Paris, Université PSL, Université Paris Cité, CNRS, 92190 Meudon, France
[99] Dipartimento di Fisica e Scienze della Terra, Università degli Studi di Ferrara, Via Giuseppe Saragat 1, 44122 Ferrara, Italy
[100] Istituto Nazionale di Fisica Nucleare, Sezione di Ferrara, Via Giuseppe Saragat 1, 44122 Ferrara, Italy
[101] Dipartimento di Fisica – Sezione di Astronomia, Università di Trieste, Via Tiepolo 11, 34131 Trieste, Italy
[102] NASA Ames Research Center, Moffett Field, CA 94035, USA
[103] Kavli Institute for Particle Astrophysics & Cosmology (KIPAC), Stanford University, Stanford, CA 94305, USA
[104] Bay Area Environmental Research Institute, Moffett Field, CA 94035, USA
[105] Minnesota Institute for Astrophysics, University of Minnesota, 116 Church St SE, Minneapolis, MN 55455, USA
[106] INAF, Istituto di Radioastronomia, Via Piero Gobetti 101, 40129 Bologna, Italy
[107] Institute Lorentz, Leiden University, PO Box 9506, Leiden 2300 RA, The Netherlands
[108] Institute for Astronomy, University of Hawaii, 2680 Woodlawn Drive, Honolulu, HI 96822, USA
[109] Department of Physics & Astronomy, University of California Irvine, Irvine, CA 92697, USA
[110] Department of Astronomy & Physics and Institute for Computational Astrophysics, Saint Mary's University, 923 Robie Street, Halifax, Nova Scotia B3H 3C3, Canada
[111] Departamento Física Aplicada, Universidad Politécnica de Cartagena, Campus Muralla del Mar, 30202 Cartagena, Murcia, Spain
[112] Université Paris Cité, CNRS, Astroparticule et Cosmologie, 75013 Paris, France
[113] Department of Computer Science, Aalto University, PO Box 15400, Espoo 00 076, Finland
[114] NRC Herzberg, 5071 West Saanich Rd, Victoria, BC V9E 2E7, Canada
[115] Ruhr University Bochum, Faculty of Physics and Astronomy, Astronomical Institute (AIRUB), German Centre for Cosmological Lensing (GCCL), 44780 Bochum, Germany
[116] Instituto de Astrofísica de Canarias (IAC), Departamento de Astrofísica, Universidad de La Laguna (ULL), 38200 La Laguna, Tenerife, Spain
[117] Université PSL, Observatoire de Paris, Sorbonne Université, CNRS, LERMA, 75014 Paris, France
[118] Université Paris-Cité, 5 Rue Thomas Mann, 75013 Paris, France

[119] Univ. Grenoble Alpes, CNRS, Grenoble INP, LPSC-IN2P3, 53, Avenue des Martyrs, 38000 Grenoble, France
[120] Department of Physics and Astronomy, University of Turku, Vesilinnantie 5, 20014 Turku, Finland
[121] Serco for European Space Agency (ESA), Camino bajo del Castillo, s/n, Urbanizacion Villafranca del Castillo, Villanueva de la Cañada 28692, Madrid, Spain
[122] Centre for Astrophysics & Supercomputing, Swinburne University of Technology, Victoria 3122, Australia
[123] ARC Centre of Excellence for Dark Matter Particle Physics, Melbourne, Australia
[124] Department of Physics and Helsinki Institute of Physics, University of Helsinki, Gustaf Hällströmin katu 2, 00014 Helsinki, Finland
[125] Oskar Klein Centre for Cosmoparticle Physics, Department of Physics, Stockholm University, Stockholm 106 91, Sweden
[126] Astrophysics Group, Blackett Laboratory, Imperial College London, London SW7 2AZ, UK
[127] Centre de Calcul de l'IN2P3/CNRS, 21 Avenue Pierre de Coubertin, 69627 Villeurbanne Cedex, France
[128] Dipartimento di Fisica, Sapienza Università di Roma, Piazzale Aldo Moro 2, 00185 Roma, Italy
[129] INFN-Sezione di Roma, Piazzale Aldo Moro 2 – c/o Dipartimento di Fisica, Edificio G. Marconi, 00185 Roma, Italy
[130] Centro de Astrofísica da Universidade do Porto, Rua das Estrelas, 4150-762 Porto, Portugal
[131] Zentrum für Astronomie, Universität Heidelberg, Philosophenweg 12, 69120 Heidelberg, Germany
[132] Dipartimento di Fisica, Università di Roma Tor Vergata, Via della Ricerca Scientifica 1, Roma, Italy
[133] INFN, Sezione di Roma 2, Via della Ricerca Scientifica 1, Roma, Italy
[134] Institute for Computational Science, University of Zurich, Winterthurerstrasse 190, 8057 Zurich, Switzerland
[135] Mullard Space Science Laboratory, University College London, Holmbury St Mary, Dorking, Surrey RH5 6NT, UK
[136] Department of Physics and Astronomy, University of California, Davis, CA 95616, USA
[137] Department of Astrophysical Sciences, Peyton Hall, Princeton University, Princeton, NJ 08544, USA
[138] Niels Bohr Institute, University of Copenhagen, Jagtvej 128, 2200 Copenhagen, Denmark

Appendix A: Colour selection parameterisation

In Tables A.1 and A.2 we report the parameterisation of *griz* and *griz*$Y_{\rm E}J_{\rm E}H_{\rm E}$ selections, respectively, described in Sect. 4.1.

Table A.1. Calibrated colour selection based on *griz* photometry. The listed colour conditions are combined through the ∨ logical operator.

Colour condition	Parameters	$z_{\rm l}$ range
$(g-r) < s\,(r-z) + c$	$s = 9.39\,z_{\rm l}^3 - 7.93\,z_{\rm l}^2 + 0.84\,z_{\rm l} + 1.69$; $c = -31.8\,z_{\rm l}^3 + 35.71\,z_{\rm l}^2 - 12.78\,z_{\rm l} + 1.04$	[0.2, 0.7]
$(g-r) < s\,(i-z) + c$	$s = 7.64\,z_{\rm l}^2 - 7.49\,z_{\rm l} + 2.75$; $c = -2.53\,z_{\rm l}^2 + 1.75\,z_{\rm l} - 0.32$	[0.2, 0.8]
$(r-i) > c$	$c = 1.28\,z_{\rm l} + 0.11$	[0.2, 0.6]
$(g-r) < s\,(r-i) + c$	$s = 2.07\,z_{\rm l}^2 - 1.75\,z_{\rm l} + 1.99$; $c = -25.25\,z_{\rm l}^3 + 28.86\,z_{\rm l}^2 - 11.72\,z_{\rm l} + 1.34$	[0.2, 0.6]
$(r-i) < s\,(r-z) + c$	$s = 8.05\,z_{\rm l}^3 - 14.37\,z_{\rm l}^2 + 6.87\,z_{\rm l} + 0.73$; $c = -8.42\,z_{\rm l}^3 + 16.11\,z_{\rm l}^2 - 9.54\,z_{\rm l} + 0.68$	[0.2, 0.8]
$(g-i) > s\,(i-z) + c$	$s = -9.17\,z_{\rm l} + 3.24$; $c = 7.07\,z_{\rm l} - 0.45$	[0.2, 0.3]
$(g-i) < s\,(r-z) + c$	$s = -47.54\,z_{\rm l}^4 + 84.36\,z_{\rm l}^3 - 53.03\,z_{\rm l}^2 + 13.64\,z_{\rm l} + 0.48$; $c = 56.05\,z_{\rm l}^4 - 107.76\,z_{\rm l}^3 + 72.88\,z_{\rm l}^2 - 21.09\,z_{\rm l} + 1.93$	[0.2, 0.8]
$(g-z) < s\,(r-z) + c$	$s = 1.70$; $c = -21.04\,z_{\rm l}^4 + 16.37\,z_{\rm l}^3 + 1.47\,z_{\rm l}^2 - 3.46\,z_{\rm l} + 0.59$	[0.2, 0.7]
$(g-r) < s\,(g-z) + c$	$s = -8.94\,z_{\rm l}^3 + 13.28\,z_{\rm l}^2 - 6.55\,z_{\rm l} + 1.73$; $c = -2.53\,z_{\rm l}^2 + 2.24\,z_{\rm l} - 0.80$	[0.2, 0.7]
$(g-r) < c$	$c = 1.46\,z_{\rm l}^2 - 1.43\,z_{\rm l} + 0.40$	[0.2, 0.5]
$(r-i) > s\,(i-z) + c$	$s = 8.45\,z_{\rm l}^2 - 6.93\,z_{\rm l} + 1.67$; $c = -2.53\,z_{\rm l}^2 + 3.48\,z_{\rm l} - 0.35$	[0.2, 0.5]
$(i-z) > c$	$c = -1.53\,z_{\rm l}^2 + 2.15\,z_{\rm l} - 0.01$	[0.2, 0.6]
$(g-z) > s\,(r-z) + c$	$s = -0.58\,z_{\rm l} - 1.42$; $c = -10.10\,z_{\rm l}^2 + 15.76\,z_{\rm l} - 0.52$	[0.2, 0.5]
$(g-i) < s\,(r-i) + c$	$s = 0.24\,z_{\rm l} + 1.53$; $c = -0.91\,z_{\rm l} + 0.33$	[0.2, 0.6]

Notes. In the first column, the colour conditions are listed. The parameters of such conditions are shown in the second column, while in the last column the $z_{\rm l}$ ranges are listed. From top to bottom, the ith row corresponds to the ith iteration of the iterative process described in Sect. 3.

Table A.2. Calibrated colour selection based on *griz*$Y_{\rm E}J_{\rm E}H_{\rm E}$ photometry. The listed colour conditions are combined through the ∨ logical operator.

Colour condition	Parameters	$z_{\rm l}$ range
$(g-i) < s\,(r-H_{\rm E}) + c$	$s = 30.81\,z_{\rm l}^4 - 79.74\,z_{\rm l}^3 + 73.28\,z_{\rm l}^2 - 28.85\,z_{\rm l} + 5.07$; $c = -31.2\,z_{\rm l}^4 + 78.62\,z_{\rm l}^3 - 71.16\,z_{\rm l}^2 + 27.57\,z_{\rm l} - 4.41$	[0.2, 1.0]
$(g-i) < s\,(z-H_{\rm E}) + c$	$s = 1.41\,z_{\rm l}^2 - 2.42\,z_{\rm l} + 2.1$; $c = -2.42\,z_{\rm l}^3 + 3.67\,z_{\rm l}^2 - 1.57\,z_{\rm l} - 0.28$	[0.2, 1.3]
$(g-r) < s\,(r-z) + c$	$s = 0.39\,z_{\rm l} + 1.33$; $c = -5.23\,z_{\rm l}^2 + 2.6\,z_{\rm l} - 0.83$	[0.2, 0.7]
$(g-Y_{\rm E}) < s\,(z-H_{\rm E}) + c$	$s = -0.01\,z_{\rm l} + 1.65$; $c = 0.37\,z_{\rm l}^2 - 1.45\,z_{\rm l} + 0.08$	[0.2, 1.5]
$(r-i) > s\,(J_{\rm E}-H_{\rm E}) + c$	$s = 1.64\,z_{\rm l} - 1.33$; $c = -0.72\,z_{\rm l}^2 + 1.49\,z_{\rm l} + 0.41$	[0.2, 0.6]
$(g-i) < s\,(z-J_{\rm E}) + c$	$s = -0.05\,z_{\rm l}^4 - 2.44\,z_{\rm l}^3 + 6.19\,z_{\rm l}^2 - 4.35\,z_{\rm l} + 2.31$; $c = -0.29\,z_{\rm l}^2 - 0.35\,z_{\rm l} - 0.21$	[0.2, 1.3]
$(g-i) < s\,(i-J_{\rm E}) + c$	$s = -2.17\,z_{\rm l}^3 + 5.01\,z_{\rm l}^2 - 3.25\,z_{\rm l} + 2.11$; $c = -2.79\,z_{\rm l}^3 + 4.06\,z_{\rm l}^2 - 2.7\,z_{\rm l} - 0.18$	[0.2, 1.1]
$(g-r) < s\,(r-H_{\rm E}) + c$	$s = -25.93\,z_{\rm l}^3 + 42.07\,z_{\rm l}^2 - 22.02\,z_{\rm l} + 4.2$; $c = 14.96\,z_{\rm l}^3 - 30.3\,z_{\rm l}^2 + 18.03\,z_{\rm l} - 3.52$	[0.2, 0.7]
$(g-i) > s\,(i-Y_{\rm E}) + c$	$s = -5.31\,z_{\rm l} + 1.99$; $c = 7.07\,z_{\rm l} - 0.45$	[0.2, 0.3]
$(g-r) < s\,(i-Y_{\rm E}) + c$	$s = -26.87\,z_{\rm l}^4 + 63.55\,z_{\rm l}^3 - 51.34\,z_{\rm l}^2 + 17.08\,z_{\rm l} - 0.8$; $c = 18.25\,z_{\rm l}^4 - 46.35\,z_{\rm l}^3 + 38.77\,z_{\rm l}^2 - 13.53\,z_{\rm l} + 1.31$	[0.2, 1.0]
$(g-r) < s\,(Y_{\rm E}-H_{\rm E}) + c$	$s = 2.07\,z_{\rm l}^2 - 2.39\,z_{\rm l} + 1.76$; $c = -10.29\,z_{\rm l}^3 + 11.18\,z_{\rm l}^2 - 4.19\,z_{\rm l} + 0.33$	[0.2, 0.7]
$(g-r) < s\,(i-H_{\rm E}) + c$	$s = -4.02\,z_{\rm l}^3 + 8.91\,z_{\rm l}^2 - 5.87\,z_{\rm l} + 1.75$; $c = -2.55\,z_{\rm l}^3 + 0.24\,z_{\rm l}^2 + 1.44\,z_{\rm l} - 0.61$	[0.2, 0.9]
$(g-z) < s\,(z-H_{\rm E}) + c$	$s = 1.43\,z_{\rm l}^4 - 5.51\,z_{\rm l}^3 + 7.29\,z_{\rm l}^2 - 3.79\,z_{\rm l} + 2.23$; $c = 0.32\,z_{\rm l}^2 - 1.55\,z_{\rm l} - 0.17$	[0.2, 1.4]
$(g-Y_{\rm E}) < s\,(i-H_{\rm E}) + c$	$s = -2.25\,z_{\rm l}^4 + 6.28\,z_{\rm l}^3 - 6.63\,z_{\rm l}^2 + 3.09\,z_{\rm l} + 1.16$; $c = -1.86\,z_{\rm l}^3 + 3.75\,z_{\rm l}^2 - 3.43\,z_{\rm l} + 0.26$	[0.2, 1.1]
$(g-z) < s\,(i-J_{\rm E}) + c$	$s = -6.33\,z_{\rm l}^4 + 15.05\,z_{\rm l}^3 - 11.67\,z_{\rm l}^2 + 3.25\,z_{\rm l} + 1.41$; $c = 8.54\,z_{\rm l}^4 - 23.53\,z_{\rm l}^3 + 22.33\,z_{\rm l}^2 - 9.11\,z_{\rm l} + 0.74$	[0.2, 1.2]
$(r-z) > s\,(i-z) + c$	$s = -5.60\,z_{\rm l}^2 + 2.31\,z_{\rm l} - 0.61$; $c = 4.69\,z_{\rm l}^2 - 0.67\,z_{\rm l} + 0.80$	[0.2, 0.7]
$(g-J_{\rm E}) < s\,(r-H_{\rm E}) + c$	$s = 2.76\,z_{\rm l}^2 - 2.91\,z_{\rm l} + 2.14$; $c = -21.51\,z_{\rm l}^3 + 23.09\,z_{\rm l}^2 - 7.14\,z_{\rm l} + 0.12$	[0.2, 0.7]
$(r-i) > s\,(z-J_{\rm E}) + c$	$s = -1.21\,z_{\rm l}^2 + 0.8\,z_{\rm l} + 0.2$; $c = 1.01\,z_{\rm l} + 0.15$	[0.2, 0.5]
$(g-z) < s\,(i-H_{\rm E}) + c$	$s = -3.66\,z_{\rm l}^4 + 12.87\,z_{\rm l}^3 - 16.26\,z_{\rm l}^2 + 7.83\,z_{\rm l} + 0.36$; $c = 6.29\,z_{\rm l}^4 - 21.87\,z_{\rm l}^3 + 26.63\,z_{\rm l}^2 - 13.19\,z_{\rm l} + 1.43$	[0.2, 1.3]
$(g-i) < s\,(r-J_{\rm E}) + c$	$s = -2.48\,z_{\rm l}^3 + 6.11\,z_{\rm l}^2 - 5.46\,z_{\rm l} + 2.59$; $c = 11.18\,z_{\rm l}^4 - 27.18\,z_{\rm l}^3 + 20.47\,z_{\rm l}^2 - 4.48\,z_{\rm l} - 0.72$	[0.2, 1.0]
$(g-z) < s\,(g-J_{\rm E}) + c$	$s = -2.16\,z_{\rm l}^3 + 5.88\,z_{\rm l}^2 - 5.06\,z_{\rm l} + 2.12$; $c = 2.33\,z_{\rm l}^3 - 6.82\,z_{\rm l}^2 + 6.18\,z_{\rm l} - 2.32$	[0.2, 1.3]
$(i-Y_{\rm E}) > s\,(z-Y_{\rm E}) + c$	$s = -0.02\,z_{\rm l} + 0.42$; $c = 2.81\,z_{\rm l}^3 - 5.05\,z_{\rm l}^2 + 3.36\,z_{\rm l} + 0.08$	[0.2, 0.8]
$(g-r) < s\,(z-J_{\rm E}) + c$	$s = 13.22\,z_{\rm l}^4 + 31.92\,z_{\rm l}^3 - 25.03\,z_{\rm l}^2 + 7.6\,z_{\rm l} + 0.42$; $c = 14.13\,z_{\rm l}^4 - 34.81\,z_{\rm l}^3 + 27.79\,z_{\rm l}^2 - 9.36\,z_{\rm l} + 0.83$	[0.2, 1.1]
$(g-i) < s\,(i-H_{\rm E}) + c$	$s = -11.75\,z_{\rm l}^4 + 33.51\,z_{\rm l}^3 - 33.07\,z_{\rm l}^2 + 12.73\,z_{\rm l} - 0.33$; $c = 10.74\,z_{\rm l}^4 - 35.01\,z_{\rm l}^3 + 37.81\,z_{\rm l}^2 - 16.31\,z_{\rm l} + 1.62$	[0.2, 1.1]
$(g-J_{\rm E}) < s\,(i-H_{\rm E}) + c$	$s = -0.03\,z_{\rm l} + 1.7$; $c = 21.04\,z_{\rm l}^4 - 48.34\,z_{\rm l}^3 + 38.51\,z_{\rm l}^2 - 13.25\,z_{\rm l} + 1.21$	[0.2, 0.9]
$(r-i) < s\,(z-J_{\rm E}) + c$	$s = -0.66\,z_{\rm l}^3 + 1.27\,z_{\rm l}^2 - 0.3\,z_{\rm l} + 1.37$; $c = 0.58\,z_{\rm l}^2 - 1.84\,z_{\rm l} - 0.38$	[0.2, 1.3]
$(i-Y_{\rm E}) < s\,(i-H_{\rm E}) + c$	$s = 2.90\,z_{\rm l} + 0.49$; $c = -6.06\,z_{\rm l} + 0.66$	[0.2, 0.3]
$(r-z) > s\,(Y_{\rm E}-J_{\rm E}) + c$	$s = 0.58\,z_{\rm l} + 0.29$; $c = 1.01\,z_{\rm l} + 0.45$	[0.2, 0.6]
$(g-r) < s\,(z-H_{\rm E}) + c$	$s = 1.1\,z_{\rm l}^3 + 0.69\,z_{\rm l}^2 - 1.14\,z_{\rm l} + 1.09$; $c = -8.67\,z_{\rm l}^3 + 9.14\,z_{\rm l}^2 - 3.35\,z_{\rm l} + 0.24$	[0.2, 0.9]
$(g-H_{\rm E}) < s\,(r-H_{\rm E}) + c$	$s = 0.78\,z_{\rm l}^2 - 1.03\,z_{\rm l} + 1.89$; $c = -13.09\,z_{\rm l}^3 + 15.15\,z_{\rm l}^2 - 5.42\,z_{\rm l} + 0.22$	[0.2, 0.7]
$(g-Y_{\rm E}) < s\,(r-J_{\rm E}) + c$	$s = 12.07\,z_{\rm l}^3 - 15.52\,z_{\rm l}^2 + 5.71\,z_{\rm l} + 1.08$; $c = -33.67\,z_{\rm l}^3 + 42.93\,z_{\rm l}^2 - 17.52\,z_{\rm l} + 1.61$	[0.2, 0.7]

Notes. The table structure is analogous to that of Table A.1.